

ORCA - Online Research @ Cardiff

This is an Open Access document downloaded from ORCA, Cardiff University's institutional repository:https://orca.cardiff.ac.uk/id/eprint/182321/

This is the author's version of a work that was submitted to / accepted for publication.

Citation for final published version:

Cai, Yi, Wang, Maolin, Zhao, Shu, Liu, Xi, Xie, Junzhong, Liu, Xing-Wu, Xu, Yao, Zhang, Jie, Zeng, Lingzhen, Qian, Fei, Gao, Zirui, Cen, Zeyan, Liu, Xingchen, Wang, Hong, Xu, Bingjun, Hutchings, Graham J., Yang, Yong, Li, Yong-Wang, Wen, Xiao-Dong and Ma, Ding 2025. Trace-level halogen blocks CO2 emission in Fischer-Tropsch synthesis for olefins production. Science 390 (6772), pp. 516-520. 10.1126/science.aea1655

Publishers page: https://doi.org/10.1126/science.aea1655

Please note:

Changes made as a result of publishing processes such as copy-editing, formatting and page numbers may not be reflected in this version. For the definitive version of this publication, please refer to the published source. You are advised to consult the publisher's version if you wish to cite this paper.

This version is being made available in accordance with publisher policies. See http://orca.cf.ac.uk/policies.html for usage policies. Copyright and moral rights for publications made available in ORCA are retained by the copyright holders.





Supplementary Materials for

Trace-level halogen blocks CO₂ emission in Fischer-Tropsch synthesis for olefins production

Yi Cai^{1,3,5,†}, Maolin Wang^{2,†}, Shu Zhao^{4,†}, Xi Liu^{6,†}, Junzhong Xie^{2,†}, Xing-Wu Liu^{2,3,*}, Yao Xu², Jie Zhang², Linzhen Zeng², Fei Qian^{1,3,5}, Zirui Gao², Zeyan Cen², Xingchen Liu¹, Hong Wang³, Bingjun Xu², Graham J. Hutchings⁷, Yong Yang^{1,3}, Yong-Wang Li³, Xiao-Dong Wen^{1,3,5,*}, Ding Ma^{2,*}

Correspondence to: Xing-Wu Liu, liuxingwu@sxicc.ac.cn, Xiao-Dong Wen, wxd@sxicc.ac.cn, Ding Ma, dma@pku.edu.cn

†These authors contributed equally to this work.

This PDF file includes:

Materials and Methods Figs. S1 to S47 Tables S1 to S18

Materials and Methods

Materials

Iron(III) nitrate nonahydrate (Fe(NO₃)₃·9H₂O), ammonium hydroxide (NH₃·H₂O), analytical-grade silica (SiO₂ (AR)), and deuterium oxide (D₂O) were purchased from Shanghai Aladdin Biochemical Technology Co., Ltd. Gas mixtures including H₂, D₂, H₂/CO, CO/Ar, H₂/CO/Ar/CH₃F, H₂/CO/Ar/CH₃Cl, H₂/CO/Ar/CH₃Br, H₂/CO/Ar/CH₃I, CH₃Cl/He, CH₃Br/He, H₂/Ar, O₂/N₂, and C₃H₆/Ar/He were supplied by Air Liquide (Tianjin) Co. Ltd. The ¹³C¹⁶O and ¹²C¹⁸O were supplied by Sigma Aldrich. All materials were used as received without further purification.

Synthesis of Catalysts

Synthesis of α -Fe₂O₃: The α -Fe₂O₃ catalyst was synthesized using a co-precipitation method. A certain amount of Fe(NO₃)₃·9H₂O was dissolved in deionized water to prepare a 2 mol/L salt solution. NH₃·H₂O was diluted with deionized water to obtain a 6 mol/L alkaline solution, serving as the precipitating agent. Both the salt and alkaline solutions were simultaneously added dropwise into a three-neck flask containing 50 mL of deionized water under mechanical stirring. Throughout the precipitation process, the pH and temperature were maintained at 8.0 ± 0.1 and 80 ± 2 °C, respectively. The resulting suspension was aged at 80 °C for 2 h, followed by centrifugation and washing three times with deionized water. The obtained solid was dried at 120 °C for 10 h, then calcined in a muffle furnace at 350 °C for 5 h under static air atmosphere with a heating rate of 2 °C/min.

Synthesis of Fe/SiO₂: The Fe/SiO₂ catalyst was synthesized via an incipient wetness impregnation method. Typically, a certain amount of Fe(NO₃)₃·9H₂O was dissolved in deionized water according to the required volume for incipient wetness impregnation of 10 g of aerosol silica (SiO₂). Subsequently, the SiO₂ support was impregnated with the above precursor solution. The slurry was stirred for 3 h, dried by evaporation, and then dried at 120 °C for 10 h. The obtained solid was calcined in a muffle furnace at 350 °C for 5 h under static air atmosphere with a heating rate of 2 °C/min.

Synthesis of ε -Fe₂C: The ε -Fe₂C catalyst was synthesized via a gas carburization method. Typically, the α -Fe₂O₃ precursor (0.5 g) was loaded into a quartz tube and first reduced to α -Fe under a flowing H₂ atmosphere (100 mL/min) at 300 °C for 10 h. The resulting α -Fe was carburized under H₂/CO (1:4) gas mixture (100 mL/min) at 185 °C for 24 h to form ε -Fe₂C. Finally, the sample was cooled to room temperature and passivated in a 0.5% O₂/N₂ gas mixture for 2 h.

Synthesis of χ -Fe₅C₂: The χ -Fe₅C₂ catalyst was synthesized via a gas carburization method. Typically, the α -Fe₂O₃ precursor (0.5 g) was loaded into a quartz tube and first reduced to α -Fe under a flowing H₂ atmosphere (100 mL/min) at 300 °C for 10 h. The obtained α -Fe was carburized under H₂/CO (1:4) gas mixture (100 mL/min) at 185 °C for 24 h. Subsequently, the gas was switched to Ar (100 mL/min), and the temperature was increased to 350 °C at a rate of 10 °C/min and maintained at 350 °C for 5 h to form χ -Fe₅C₂. Finally, the sample was cooled to room temperature and passivated in a 0.5% O₂/N₂ gas mixture for 2 h.

Synthesis of θ -Fe₃C: The θ -Fe₃C catalyst was synthesized via a gas carburization method. Typically, the α -Fe₂O₃ precursor (0.5 g) was loaded into a quartz tube and first reduced to α -Fe under a flowing H₂ atmosphere (100 mL/min) at 300 °C for 10 h. The obtained α -Fe was carburized under H₂/CO (1:4) gas mixture (100 mL/min) at 185 °C for 24 h. Subsequently, the gas was switched to Ar (100 mL/min), and the temperature increased to 500 °C at 30 °C min⁻¹ and maintained at 500 °C for 1 h to form θ -Fe₃C. Finally, the sample was cooled to room temperature and passivated in a 0.5% O₂/N₂ gas mixture for 2 h.

Synthesis of h-Fe₇C₃: The h-Fe₇C₃ catalyst was synthesized using a ball milling method. Nano-iron powder and graphite-carbon were weighed according to the atomic ratio of Fe:C = 7:3 and loaded into a ball milling vessel, and the whole process was conducted in a glovebox. h-Fe₇C₃ was obtained after continuous milling at a rotational speed of 600 rpm for 30 h.

Synthesis of Fe₃O₄: The Fe₃O₄ catalyst was synthesized via treatment under a water-gas shift reaction atmosphere. Typically, the α -Fe₂O₃ precursor (0.5 g) was loaded into a quartz tube and treated under H₂O/CO/Ar = 20/24/56 gas mixture (100 mL/min) at 300 °C for 2 h to obtain Fe₃O₄.

Characterization of Catalysts

All characterizations of χ -Fe₅C₂-spent and χ -Fe₅C₂-Br-spent catalysts were conducted on samples collected 80–100 h after reaching steady-state in FTS reaction.

Synchrotron X-ray Diffraction (XRD): The experiment was conducted at the BL02U2 beamline at the Shanghai Synchrotron Radiation Facility (SSRF), which operated at 3.5 GeV with a current of 220.75 mA. The incident X-ray energy E = 19.000 keV ($\lambda = 0.6543$ Å), with a photon flux of 5.5×10^{12} photon/s at 10.0 keV. The beam size was 200 (H) × 100 (V) μ m², and the beam divergence was 200 (H) × 60 (V) μ rad². Data was collected using a Pilatus 2M detector, and LaB₆ powder was used for calibration of distance between sample holder and detector. The sample was loaded into a glass capillary with o.d. = 1 mm and i.d. = 0.8 mm inside a glovebox and sealed by melting both sides of the capillary. During experiment, the sample was placed on the sample holder, under ambient temperature and pressure.

X-ray Absorption Spectroscopy (XAS): The experiments were conducted at the Br K-edge (13474 eV) on beamline BL01B1 at SPring-8, which operated at 8.0 GeV with a current of 99.5 mA. Si (111) double crystal monochromator (DCM) was used. The photon flux at 10.0 keV was 9×10^{10} photons/s with a beam size of 4.0 (H) \times 1.0 (V) mm² (vertically focused by Rh-coated mirror). Data were acquired in fluorescence mode (19-element Germanium solid-state detector) for Br K-edge. Step-scan mode ($k_{\text{max}} = 16$ –20) was set up for experiments. NaBrO₃ powder was used for energy calibration. The catalyst was pretreated then carefully transferred to a glovebox, tableted, and sealed with Kapton tape. Data was collected at ambient temperature and pressure.

The experiments were conducted at the Fe K-edge (7112 eV) on beamline BL20U1 at Shanghai Synchrotron Radiation Facility (SSRF), which operated at 3.5 GeV with a current of 220.75 mA. Si (111) double crystal monochromator (DCM) was used. The photon flux at 10.0 keV was 5×10^{12} photon/s with a beam size of 80 (H) \times 20 (V) μ m². Data was acquired in transmission mode (ionization chamber) for Fe K-edge. Step-scan mode ($k_{max} = 16-20$) was set up for experiments. Fe foil was used for energy calibration. The catalyst was pretreated then

carefully transferred to a glovebox, tableted, and sealed with Kapton tape. Data was collected at ambient temperature and pressure.

The XAS data were processed and analyzed using Demeter software package (48). For XANES and XAFS data, a linear function was subtracted from the pre-edge region, then the edge jump was normalized using Athena software. The edge energy (E_0) was selected as the inflection point of absorption edge. The $\chi(k)$ data were isolated by subtracting a smooth, third polynomial approximating the absorption background of an isolated atom. The k^2 -weighted $\chi(k)$ data were Fourier transformed after applying a Hanning window ($dk = 1 \text{ Å}^{-1}$). The global amplitude N (degeneration), R (path length), ΔE_0 (energy shift), σ^2 (Debye-Waller factor) were obtained by nonlinear fitting with least-squares refinement, of the EXAFS equation to the Fourier-transformed data in R-space using Artemis software. Detailed fitting settings and parameters were listed at tables of curve fittings.

X-ray Photoelectron Spectroscopy (XPS): The experiment was conducted using an AXIS Supra X-ray photoelectron spectrometer (Kratos Analytical Ltd.) with an Al K_{α} radiation source. The pretreated catalyst was transferred into the XPS chamber without being exposed to air. Near ambient pressure XPS (NAP-XPS) measurements were performed in an in-situ reaction chamber equipped with a PHOIBOS 150NAP and a 1D-DLD analyzer. The sample powder was tightly pressed onto aluminum foil fixed to a tantalum plate to ensure conductivity and then transferred into the NAP-XPS chamber. The sample was first treated in a high-pressure chamber with Ar at 400 °C for 1 h (with a heating rate of 10 °C/min). After cooling to room temperature, the sample was transferred to the analysis chamber. Spectra were collected at certain temperatures, under the atmosphere of 1 mbar H₂O. The ramping rate was 5 °C/min and each temperature was maintained for 20 min.

Synchrotron XPS: The experiment was conducted on BL02B01 at Shanghai Synchrotron Radiation Facility (SSRF). The treated sample was sealed in a surface-punctured button cell in a glove box, securely sealed with tape, and then transferred to the XPS chamber in vacuum. The sealing tape was removed using an internal mechanical arm to expose the sample. Spectra focused on the Br 3d, C 1s, O 1s, and Fe 2p regions. The energy of the incoming X-ray was

adjusted to maintain the kinetic energy (K.E. = 300 & 700 eV) of the detected photoelectrons, allowing for variable detection depths of different elements.

Background of the spectrum was subtracted using a Shirley background. Since the sample was conductive and loaded on aluminum foil, the peak positions were not aligned. Peak fitting was performed using CasaXPS (49). O 1s peak was fitted using the 530.20 eV as reference for O_{lattice}, 531.57 eV as reference for OH_{ads}, 533.05 eV as reference for H₂O_{ads} and 535.16 eV as reference for H₂O_g. All peaks were fitted using a Gaussian-Lorentzian type of peak.

Diffuse Reflectance Infrared Fourier-Transform Spectroscopy (DRIFTS): The experiment was performed in home-made reaction cell on VERTEX 70 spectrometer equipped with a liquid nitrogen cooled mercury-cadmium-telluride (MCT) detector and Praying Mantis diffuse reflection accessory (Harrick Scientific). About 50 mg α -Fe₂O₃ was first loaded in the reaction cell, then pretreated at 300 °C with 10 mL/min CO/H₂O/Ar = 0.5/0.5/99 to get Fe₃O₄. Then the gas was switched to 10 mL/min Ar (for Fe₃O₄) or 10 mL/min 500 ppm CH₃Br/He (for Fe₃O₄-Br) for 1 h. After purging in Ar for 30 min, the temperature was elevated to 400 °C and held for 60 min. After that, the sample was cooled to 300 °C and background was collected. The gas was switched to 10 mL/min H₂O/Ar = 0.5/99.5 and held for 15 min until the spectrum stopped changing, then switched back to 10 mL/min Ar. Data was collected throughout the whole process.

Mössbauer Spectroscopy (MES): Mössbauer spectroscopy measurements were conducted in an MR-351 constant-acceleration Mössbauer spectrometer (FAST, Germany) driven with a triangular reference signal at 10 K. The radioactive source was ⁵⁷Co in the Rh matrix. The velocity was calibrated using an α-Fe foil as the reference. Data analysis was performed using the MossWinn 4.0 software package. The composition of the Fe phase was identified based on isomer shift (IS), quadrupole splitting (QS), and magnetic hyperfine field (H_{hf}) parameters. The relative contents of the different iron phases in the sample were quantified by integrating the adsorption peak areas corresponding to the Fe phase in the catalyst.

High-sensitivity Low-energy ion scattering (HS-LEIS): HS-LEIS was performed on Ion-TOF Qtac100 to analyze the surface elemental composition of the catalyst. He⁺ with a 3 keV kinetic energy was used as the probe ions, and Ne⁺ with a 5 keV kinetic energy served as the etching ion beam. Before testing, the catalysts were treated under Ar at 300 °C (ramping rate = 10 °C/min) for 60 min in the high-pressure reaction cell (10 mL/min, 1 bar). After cooling to room temperature under Ar, the sample was transferred to the high-vacuum chamber for HS-LEIS analysis.

Transmission Electron Microscopy (TEM): TEM was performed using an FEI Talos 200A microscope operated at an acceleration voltage of 200 kV. The particle size distribution for each sample was determined by measuring over 100 individual nanoparticles from representative TEM images using the Nano Measurer 1.2 software. Catalyst samples were prepared by dispersing the powder in ethanol via ultrasonication, followed by drop casting the resulting suspension onto copper grids coated with holey carbon films. The grids were then dried at room temperature before measurement.

Scanning Transmission Electron Microscopy (STEM): STEM and energy-dispersive X-ray spectroscopy (EDS) analyses were performed on an aberration-corrected JEM-ARM200F (JEOL) field-emission electron microscope, equipped with a JEOL JED2300 EDS detector, operated at an acceleration voltage of 200 kV. High-angle annular dark-field scanning transmission electron microscopy (HAADF-STEM) images were collected using an annular dark-field detector with a collection angle range of 54–220 mrad and a convergence semi-angle of 20.6 mrad. The STEM probe current was maintained at 17 pA, and the probe size was approximately 0.133 nm. Catalyst samples were prepared by dispersing the powder in ethanol via ultrasonication, followed by drop casting the resulting suspension onto copper grids coated with holey carbon films. The grids were then dried at room temperature before measurement.

Ion Chromatography (IC): IC was used to quantify the bromide content in the solid and liquid samples. The analysis was performed using a Metrohm 881 Compact IC Pro chromatograph equipped with a Metrosep A Supp 7-250/4.0 analytical column and chemical suppression conductivity detector (Metrohm Suppressor Module). 3.6 mmol/L Na₂CO₃ solution was used as an eluent, operated at a flow rate 0.7 mL/min. The injection volume was $20 \,\mu$ L, and the column temperature was maintained at 45 °C. Bromide on the solid catalyst was

collected via thermal combustion hydrolysis. The aqueous products were diluted 10-fold prior to chromatographic analysis. Oil phase products were first extracted using an equal volume of ultrapure water, followed by 2-fold dilution prior to measurement. All samples were filtered through a $0.22 \,\mu m$ membrane filter before injection. External calibration was performed using standard bromide solutions.

N₂ Adsorption-desorption Isotherms: Nitrogen adsorption-desorption isotherms were measured at -196 °C (liquid nitrogen temperature) using a Micromeritics ASAP 2040 Surface Area and Porosity Analyzer. Prior to analysis, the samples were degassed under dynamic vacuum at 200 °C for 6 h to remove surface-adsorbed moisture and volatile species.

Transient Kinetic Analysis (TKA): Pretreatment of χ -Fe₅C₂ catalyst: 50 mg of passivated χ -Fe₅C₂ was loaded into a quartz tube with an *i. d.* = 3 mm, using CO/H₂/Ar = 24/72/4 (feed gas first passed through a stainless tube heated to 220 °C to remove Ni(CO)₄) at a heating rate of 10 °C/min to 280 °C and held for 30 min, then switched to Ar. The temperature was further increased to 320 °C and maintained for 30 min to remove surface adsorbates.

Pretreatment of χ -Fe₅C₂-Br catalyst: catalyst for TKA experiment was prepared by running the catalyst under syngas containing 20 ppm CH₃Br at 300 °C, 10 bar, with a space velocity (SV) of 12000 mL·g_{cat}-1·h⁻¹ and H₂/CO = 2 for 50 h, then cooled to room temperature and passivated in a 0.5% O₂/N₂ gas mixture for 2 h. Passivated catalyst was pretreated before experiments: 50 mg of χ -Fe₅C₂-Br catalyst was loaded into a quartz tube with an inner diameter of 3 mm, using CO/H₂/Ar = 24/72/4 (feed gas first passed through a stainless tube heated to 220 °C to remove Ni(CO)₄) at a heating rate of 10 °C/min to 280 °C and held for 30 min, then switched to Ar. The temperature was further increased to 320 °C and maintained for 30 min to remove surface adsorbates.

Pretreatment of Fe₃O₄ catalyst: 100 mg of α -Fe₂O₃ was loaded into a quartz tube, heated at 10 °C/min in Ar to 280 °C, and switched to 20 mL/min CO/H₂O/Ar = 2.5/2.5/95 for 2 h. The temperature then increased to 320 °C and maintained for 30 min to remove surface adsorbates.

Pretreatment of Fe₃O₄-Br catalyst: after the treatment procedure above, the Fe₃O₄ catalyst was cooled to 300 °C and maintained at that temperature. It was then switched to 10 mL/min

500 ppm CH₃Br/He until CH₃Br was no longer consumed, followed by switching to 20 mL/min Ar purging for 30 min. The temperature then increased to 320 °C and maintained for 30 min to remove surface adsorbates.

After pretreatment, TKA experiments were conducted. Detailed experimental conditions were noted in each Figures. The products were detected by online mass spectrometer (MS, OMNI Star GSD320, Pfeiffer) using the following MS signals: H_2 (m/Z = 2), HD (m/Z = 3), $He\&D_2$ (m/Z = 4), CH_4 (m/Z = 15), CH_2 (m/Z = 17&18), CH_2 (m/Z = 18), CH_3 (m/Z = 18), CH_4 (m/Z = 18), CH_4

Pulse Experiments: C_3H_6 pulse transient hydrogenation and CO pulse experiments were performed on an AMI-300 instrument equipped with a thermal conductivity detector (TCD) and an MS (OMNI Star GSD320, Pfeiffer). 100 mg catalyst was loaded into a U-tube reactor and pretreated using CO/H₂/Ar = 24/72/4 (feed gas first passed through a stainless tube heating to 220 °C to remove Ni(CO)₄) at a heating rate of 10 °C/min to 280 °C and held for 30 min. For the C_3H_6 pulse experiments, the gas feed was switched to Ar (20 mL/min) after pretreatment. The temperature was further increased to 320 °C and maintained for 30 min to remove surface adsorbates. Subsequently, the feed was switched to pure H_2 (20 mL/min), and C_3H_6 was pulsed into the system to perform transient hydrogenation. The products were detected by MS using the following signals: C_3H_6 (m/Z = 42) and C_3H_8 (m/Z = 44). For the CO pulse experiment, the same procedure was followed by switching the feed gas to Ar (20 mL/min). The temperature was raised to 320 °C and maintained for 30 min to remove surface adsorbates. Subsequently, CO was pulsed into the system to carry out the pulse reaction. The products were detected by MS using the following signals: CO (m/Z = 28) and CO₂ (m/Z = 44). All signals recorded were normalized to signal of Ar, and calibration factors were determined

from measuring the standard gases of known concentrations after the experiments. The mass-to-charge axis was calibrated in Faraday detection mode prior to each experiment.

Catalytic Performance Evaluation

Analysis and Quantification Method: The catalytic performances of different catalysts for syngas conversion were evaluated in a continuous-flow fixed-bed microreactor equipped with four stainless steel tubes and inserted stainless-steel sieves with thermocouples to monitor the reaction temperature. 0.1 g catalyst (60-80 mesh) was diluted with 0.6 g silicon carbide (SiC, 60-80 mesh) and loaded into the constant temperature zone of the reactor. Prior to the catalytic reaction, the catalyst was in situ activated in feed gas at 280 °C for 6 h. The reaction conditions were typically 300 °C, 5 bar, syngas with $H_2/CO = 2$ (CO/ $H_2/Ar = 32/64/4$), co-feeding 20 ppm CH₃Br, and space velocity (SV) of 12000 mL· g_{cat} -1·h-1 unless otherwise specified. Ar was used as an internal standard to calculate the CO conversion and selectivity of products in the outlet gas. After passing through a hot trap (160 °C) and cold trap (0 °C), the outlet gas was analyzed online using an Agilent 7890B gas chromatograph (GC) with one thermal conductivity detector (TCD) and two flame ionization detectors (FID).

The gases H₂, CO₂, Ar, and CO were analyzed using a combination of PLOT/Q, 5 Å molecular sieve, and Haysep Q capillary columns and detected by a TCD with He as the carrier gas. C₁-C₄ hydrocarbons were analyzed using a Gaspro capillary column coupled with a DM-1 backflush column and detected by an FID with N₂ as the carrier gas. C₄-C₇ hydrocarbons were analyzed using a PONA capillary column connected to an FID with N₂ as carrier gas. The aqueous phase, liquid oil, and solid wax products were collected from the cold trap and hot trap and subsequently analyzed offline using an HP-PONA capillary column.

Calculation of conversion, selectivity, yield, and space-time yield of products: The CO conversion and product selectivity of the catalysts were calculated on a carbon atom basis. The mass, carbon, and oxygen balances were maintained within the range of (100 ± 5) %. All experimental results were based on at least three repeated experiments performed under the same reaction conditions, demonstrating that the catalyst showed good reproducibility.

The CO conversion, product selectivity, and product yield were calculated using the following equations:

The CO conversion (X_{CO}) , was calculated by

$$X_{CO} = \frac{\frac{CO_{inlet}}{Ar_{inlet}} - \frac{CO_{outlet}}{Ar_{outlet}}}{\frac{CO_{inlet}}{Ar_{outlet}}} \times 100\%$$

The CO₂ selectivity (S_{CO_2}) was calculated by

$$S_{CO_2} = \frac{\frac{CO_{2outlet}}{Ar_{outlet}}}{\frac{CO_{inlet}}{Ar_{inlet}} - \frac{CO_{outlet}}{Ar_{outlet}}} \times 100\%$$

The carbon-based hydrocarbon selectivity $(S_{C_xH_y})$ was calculated by

$$S_{C_x H_y} = \frac{\frac{x C_x H_{y \ outlet}}{A r_{outlet}}}{\frac{CO_{inlet}}{A r_{inlet}} - \frac{CO_{outlet}}{A r_{outlet}}} \times 100\%$$

The olefins yield ($Y_{olefins}$) was calculated by

$$Y_{olefins} = X_{CO} \times S_{olefins} \times 100\%$$

The CO consumption rate per gram of catalyst (R_{CO}) was calculated by

$$R_{CO} = \frac{SV \times X_{CO} \times C_{co\ concentration}}{22400}$$

Where SV is the space velocity (mL·g_{cat}-1·h⁻¹), $C_{co\ concentration}$ denotes the molar concentration of CO in feed syngas.

The catalyst space-time yield for olefins $(STY_{olefins})$ was calculated by

$$STY_{olefins} = R_{CO} \times S_{olefins}$$

In the above equations, CO_{inlet} , CO_{outlet} , Ar_{inlet} and Ar_{outlet} represent the inlet and outlet molar flows of CO and Ar, $CO_{2outlet}$ and $C_xH_{y\ outlet}$ represent the outlet molar flows of CO₂ and C_xH_y . S_{CO_2} , $S_{C_xH_y}$, and $S_{olefins}$ denote the selectivity based on carbon atoms.

Calculation of Chain Growth Probability: The chain growth probability (α) was calculated according to Anderson-Schulz-Flory distribution using the following equations:

$$\left(\frac{W_n}{n}\right) = (1 - \alpha)^2 \alpha^{(n-1)}$$

Where n is the carbon number of products, W_n is the mass fraction of the hydrocarbons with a carbon number of n, and α is chain growth probability.

Above equation for α calculation can be rewritten as:

$$ln\left(\frac{W_n}{n}\right) = (n-1)ln\alpha + 2ln(1-\alpha)$$

By plotting $\ln\left(\frac{W_n}{n}\right)$ versus n (carbon number), and the chain growth probability α can be obtained from the slope of the fitted line, which corresponds to $\ln \alpha$.

Computational Method

All first-principles calculations were conducted using density functional theory (DFT), as implemented in the Vienna *ab initio* Simulation Package (VASP) (50–51). The electron exchange-correlation interactions were treated using the generalized gradient approximation (GGA) with the Perdew-Burke-Ernzerhof functional (PBE) (52). The Kohn-Sham equations were solved iteratively using a plane-wave basis set with a kinetic energy cutoff of 400 eV. Brillouin zone integrations were performed using a Monkhorst-Pack k-point mesh of ($2 \times 2 \times 1$). The convergence criteria for the electronic self-consistent iteration and force were set to 10^{-4} eV and 0.02 eV/Å, respectively. Transition states and reaction pathways were identified using the climbing image nudged elastic band (CI-NEB) method (53–54). To account for long-range dispersion interactions, the DFT-D3 correction scheme was employed in the evaluation of adsorption energies. Bader charge analysis was applied to evaluate the charge transfer of the system (55–56).

The χ -Fe₅C₂ (100) surface was modeled using a $p(2 \times 2)$ supercell consisting of 6 atomic layers, in which the top two layers were allowed to relax. For the Fe₃O₄(111) surface, a Fe_{oct}-terminated primitive (1 × 1) slab model was constructed with 12 atomic layers, and the bottom four layers were fixed. The vacuum gap was set as 15 Å to avoid the interaction between periodic images. Reaction energies and energy barriers were calculated by the following expressions: $E_r = E(FS) - E(IS)$ and $E_a = E(TS) - E(IS)$, where E(IS), E(FS) and E(TS) are the

energies of the corresponding initial state (IS), final state (FS), and transition state (TS), respectively.

In theoretical calculations, the surface bromine coverage $(\theta_{\rm Br})$ on the catalyst surface is defined as the ratio of the number of surface bromine atoms $(N_{\rm Br})$ to the number of surface iron atoms $(N_{\rm Fe})$ exposed on either the Fe₃O₄ or χ -Fe₅C₂ slab models: $\theta_{Br} = \frac{N_{Br}}{N_{Fe}}$.

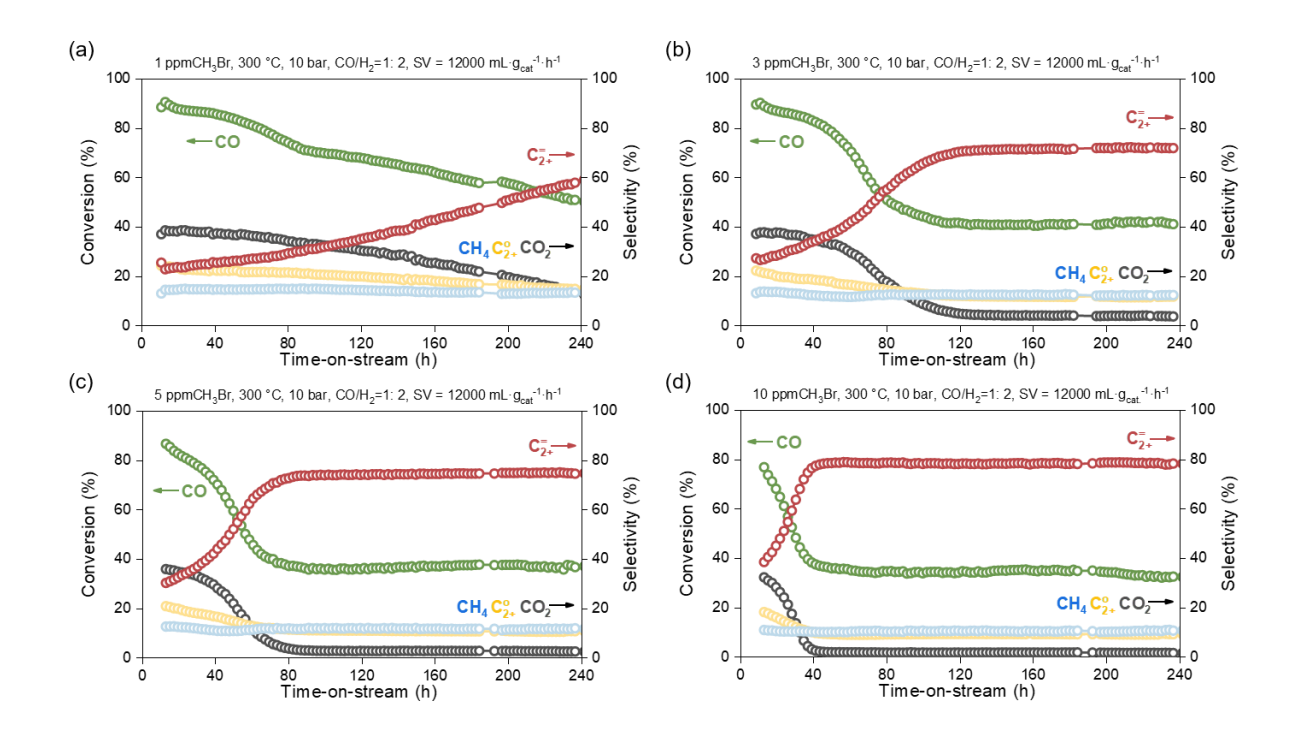


Fig. S1.

CO conversion and product selectivity over χ -Fe₅C₂ catalyst under syngas co-feeding with different CH₃Br concentrations of 1 ppm (a), 3 ppm (b), 5 ppm (c), and 10 ppm (d). Reaction conditions: 100 mg catalyst, T = 300 °C, P = 10 bar, SV = 12000 mL·g_{cat}-1·h⁻¹, H₂/CO = 2 (molar ratio), co-feeding CH₃Br (1–10 ppm). Catalysts were pretreated at 280 °C and 1 bar for 6 h, SV = 12000 mL·g_{cat}-1·h⁻¹, H₂/CO = 2.

Note: To systematically investigate the effect of CH₃Br concentration on the catalytic performance of χ -Fe₅C₂ catalyst, we co-fed CH₃Br at different concentrations (1, 3, 5, and 10 ppm) under conditions of 300 °C, 10 bar and H₂/CO = 2, and continuously monitored the evolution of the CO conversion rate and the selectivity of the main products over time. The results show that with an increase in CH₃Br concentration, the selectivity of CO₂ and CH₄ decreases significantly, while the selectivity of C₂₊ olefins continues to increase. In the condition of co-feeding 10 ppm CH₃Br, the selectivity of C₂₊ olefins rapidly increased to 80%, the selectivity of CO₂ was stably inhibited to about 1.7% and had good stability. More importantly, even 1-3 ppm CH₃Br can effectively suppress the selectivity of CO₂ to 3.9% and

promote the production of olefins. This series of experiments clearly shows that trace amounts of CH₃Br can significantly regulate the FTS reaction performance of the χ -Fe₅C₂ catalyst.

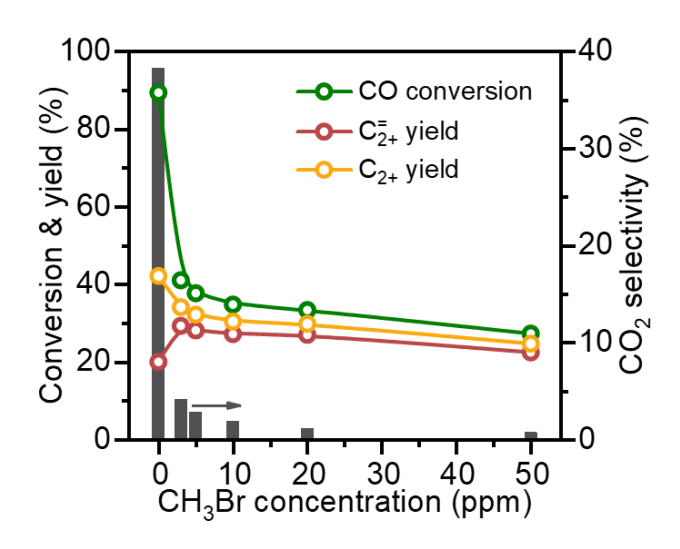


Fig. S2. Dependence of CO conversion, yields of C₂₊ olefins, hydrocarbons, and CO₂ selectivity on the co-feeding concentration of CH₃Br (0–50 ppm) over χ -Fe₅C₂. Reaction conditions: 100 mg catalyst, T = 300 °C, P = 10 bar, SV = 12000 mL·g_{cat}-1·h⁻¹, H₂/CO = 2, co-feeding 0–50 ppm CH₃Br. Catalysts were pretreated at 280 °C and 1 bar for 6 h, SV = 12000 mL·g_{cat}-1·h⁻¹, H₂/CO

= 2.

Note: With increasing CH₃Br co-feeding concentration, both CO conversion and CO₂ yield decreased significantly. In sharp contrast, the C₂- hydrocarbon yield exhibited only a slight decline. Since all experiments were conducted under identical conditions, this indicates that Br co-feeding strongly inhibited the rate of CO₂ formation while having a much milder inhibitory effect on hydrocarbon formation. Specifically, at 10 ppm CH₃Br co-feeding, the CO₂ formation rate decreased to 2% of its original value, whereas the hydrocarbon formation rate remained relatively high at 72% of the original value, demonstrating the highly selective inhibitory effect of Br on CO₂ production over hydrocarbon synthesis (Table S3). This suggests that the majority of the decrease in CO conversion is attributable to the reduction in CO₂ formation, and the catalyst maintains high efficiency in Fischer-Tropsch synthesis.

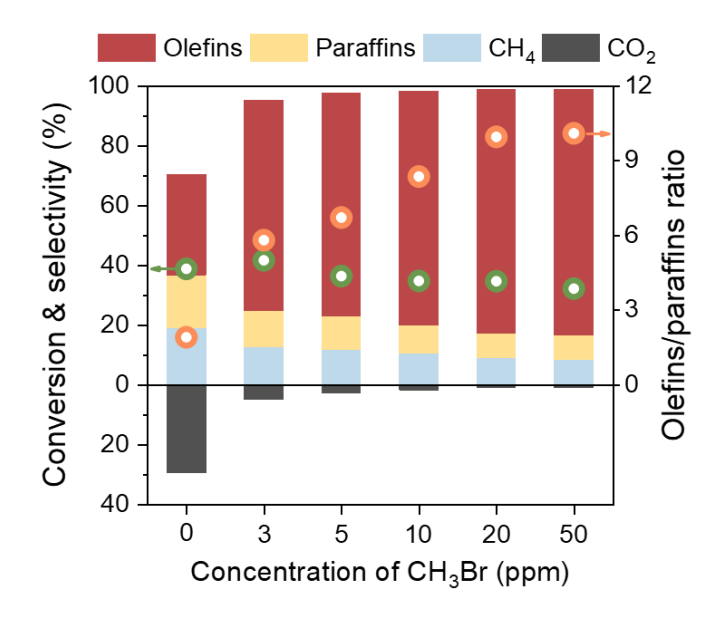
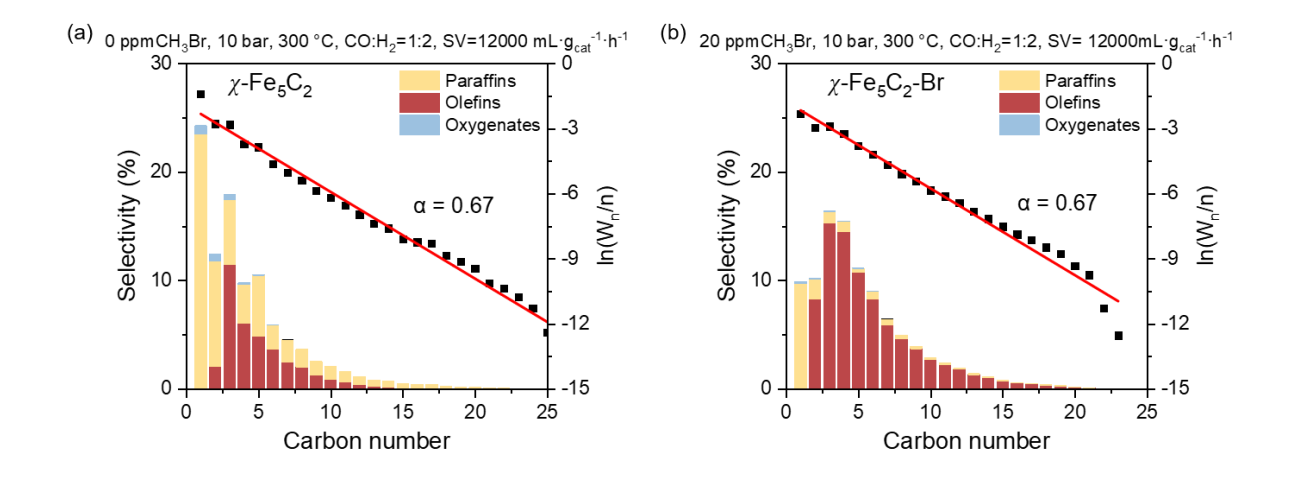


Fig. S3.

CO conversion, product selectivity, and olefins/paraffins ratio over χ -Fe₅C₂ catalyst at comparable CO conversion levels (30–40%) with different co-feeding CH₃Br concentrations (0–50 ppm). Reaction conditions: 100 mg catalyst, T = 300 °C, P = 10 bar, SV = 12000–60000 mL·g_{cat}-1·h-1, H₂/CO = 2, co-feeding 0–50 ppm CH₃Br. Catalysts were pretreated at 280 °C and 1 bar for 6 h, SV = 12000 mL·g_{cat}-1·h-1, H₂/CO = 2.

Note: Clearly, without CH₃Br co-feeding, when we control CO conversion at 38.8% (similar level with those with co-feeding), the CO₂ selectivity is 29.6% and the o/p ratio is 1.9. Thus, even at comparable CO conversions, the inclusion of trace amounts of CH₃Br in the feed is able to suppress the CO₂ selectivity by more than an order of magnitude.



Detailed distribution of hydrocarbon products obtained over χ -Fe₅C₂ (a) and χ -Fe₅C₂-Br (b) catalysts. Reaction conditions: 100 mg catalyst, T = 300 °C, P = 10 bar, SV = 12000 mL·g_{cat}⁻¹·h⁻¹, H₂/CO = 2. χ -Fe₅C₂, syngas without CH₃Br. χ -Fe₅C₂-Br, co-feeding 20 ppm CH₃Br. Catalysts were pretreated at 280 °C and 1 bar for 6 h, SV = 12000 mL·g_{cat}⁻¹·h⁻¹, H₂/CO = 2 (χ -Fe₅C₂, syngas without CH₃Br; χ -Fe₅C₂-Br, co-feeding 20 ppm CH₃Br).

Fig. S4.

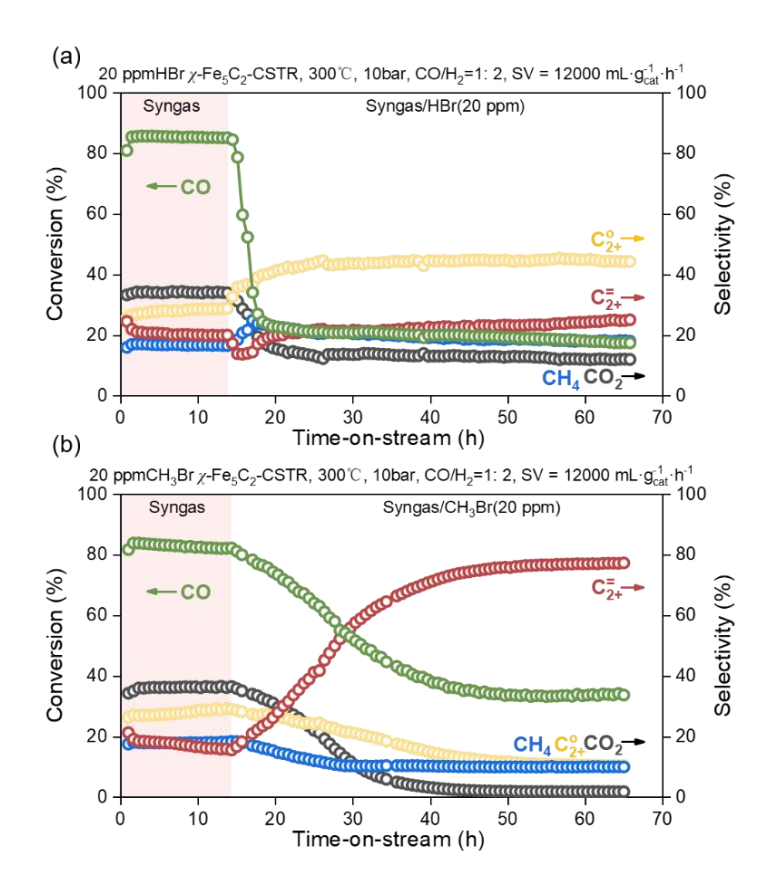


Fig. S5.

CO conversion and product selectivity over χ -Fe₅C₂ catalyst under syngas co-feeding with 20 ppm HBr (a) and 20 ppm CH₃Br (b). Experiments were performed in a continuously stirred tank reactor (CSTR). Reaction conditions: 300 mg catalyst, T = 300 °C, P = 10 bar, SV = 12000 mL·g_{cat}-1·h⁻¹, H₂/CO = 2, co-feeding 20 ppm CH₃Br or HBr, reactor volume = 100 mL, with 50 mL of liquid paraffin initially added as the slurry medium, stirring speed = 1300 rpm.

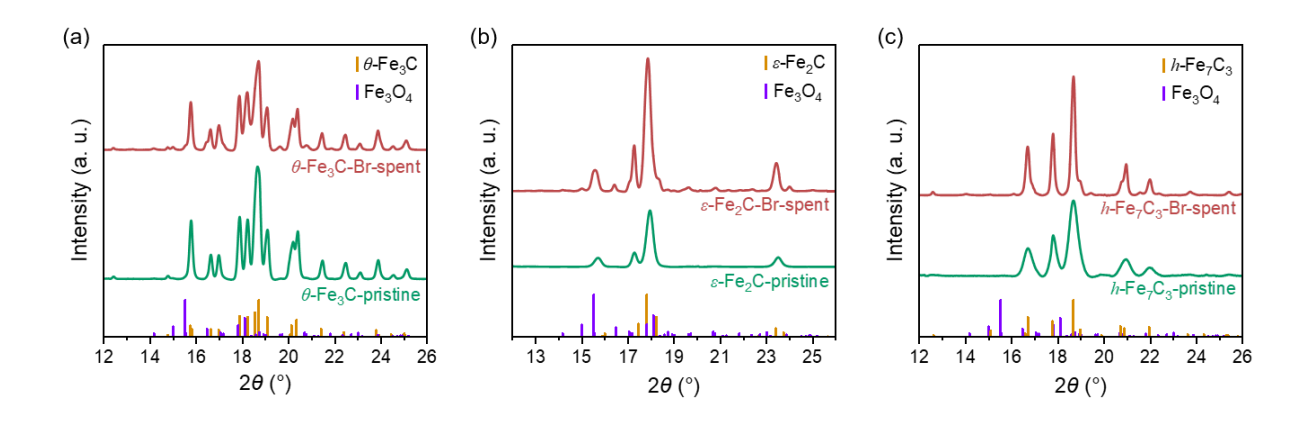


Fig. S6. Synchrotron XRD of pristine and spent θ -Fe₃C (a), ε -Fe₂C (b), and h-Fe₇C₃ (c). Reaction conditions: 100 mg catalysts, T = 300 °C, P = 10 bar, SV = 12000 mL·g_{cat}-1·h⁻¹, H₂/CO = 2, co-feeding 20 ppm CH₃Br. Catalysts were pretreated at 280 °C and 1 bar for 6 h, SV = 12000 mL·g_{cat}-1·h⁻¹, H₂/CO = 2.

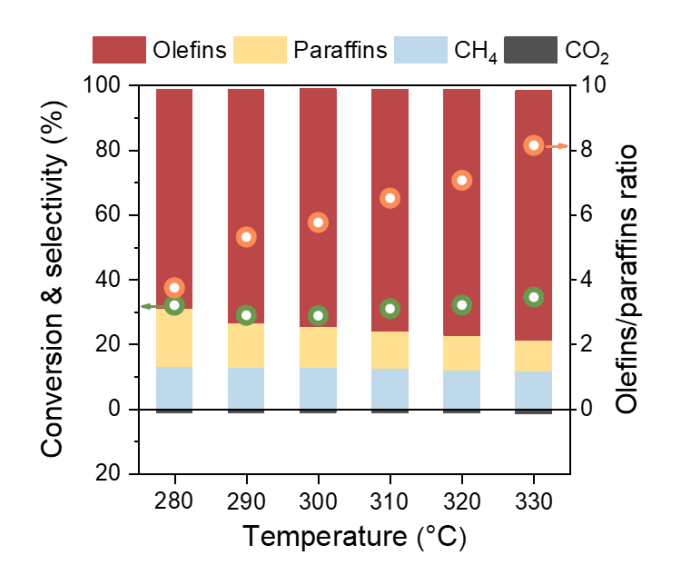


Fig. S7.

CO conversion, product selectivity, and olefins/paraffins ratio at different reaction temperatures over χ -Fe₅C₂-Br catalyst. Reaction conditions: 100 mg catalyst, T = 280-330 °C, P = 20 bar, SV = 12000 mL·g_{cat}-1·h⁻¹, H₂/CO = 2, co-feeding 20 ppm CH₃Br. Catalysts were pretreated at 280 °C and 1 bar for 6 h, SV = 12000 mL·g_{cat}-1·h⁻¹, H₂/CO = 2, co-feeding 20 ppm CH₃Br.

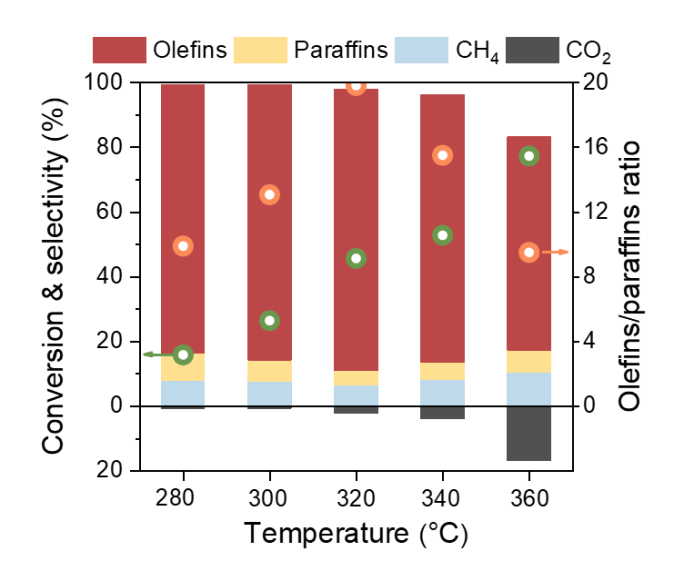


Fig. S8.

CO conversion, product selectivity, and olefins/paraffins ratio at different reaction temperatures over χ -Fe₅C₂-Br catalyst. Reaction conditions: 100 mg catalyst, T = 280-360 °C, P = 5 bar, SV = 12000 mL·g_{cat}-1·h⁻¹, H₂/CO = 2, co-feeding 20 ppm CH₃Br. Catalysts were pretreated at 280 °C and 1 bar for 6 h, SV = 12000 mL·g_{cat}-1·h⁻¹, H₂/CO = 2, co-feeding 20 ppm CH₃Br.

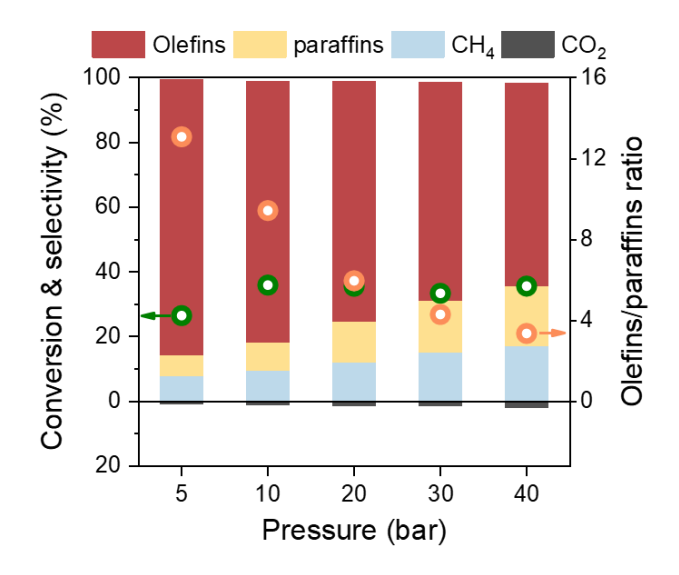


Fig. S9.

CO conversion, product selectivity, and olefins/paraffins ratio at varying reaction pressures over χ -Fe₅C₂-Br catalyst. Reaction conditions: 100 mg catalyst, T = 300 °C, P = 5–40 bar, SV = 12000 mL·g_{cat}-1·h-1, H₂/CO = 2, co-feeding 20 ppm CH₃Br. Catalysts were pretreated at 280 °C and 1 bar for 6 h, SV = 12000 mL·g_{cat}-1·h-1, H₂/CO = 2, co-feeding 20 ppm CH₃Br.

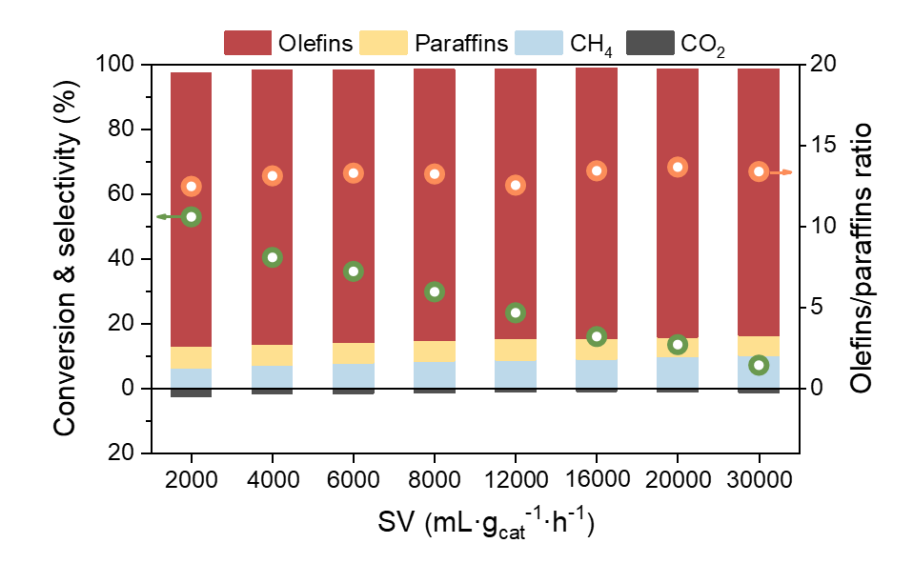


Fig. S10. CO conversion, product selectivity, and olefins/paraffins ratio at different space velocities over χ -Fe₅C₂-Br catalysts. Reaction conditions: 100 mg catalyst, T=300 °C, P=5 bar, SV = 2000–30000 mL·g_{cat}-¹·h-¹, H₂/CO = 2, co-feeding 20 ppm CH₃Br. Catalysts were pretreated at 280 °C and 1 bar for 6 h, SV = 12000 mL·g_{cat}-¹·h-¹, H₂/CO = 2, co-feeding 20 ppm CH₃Br.

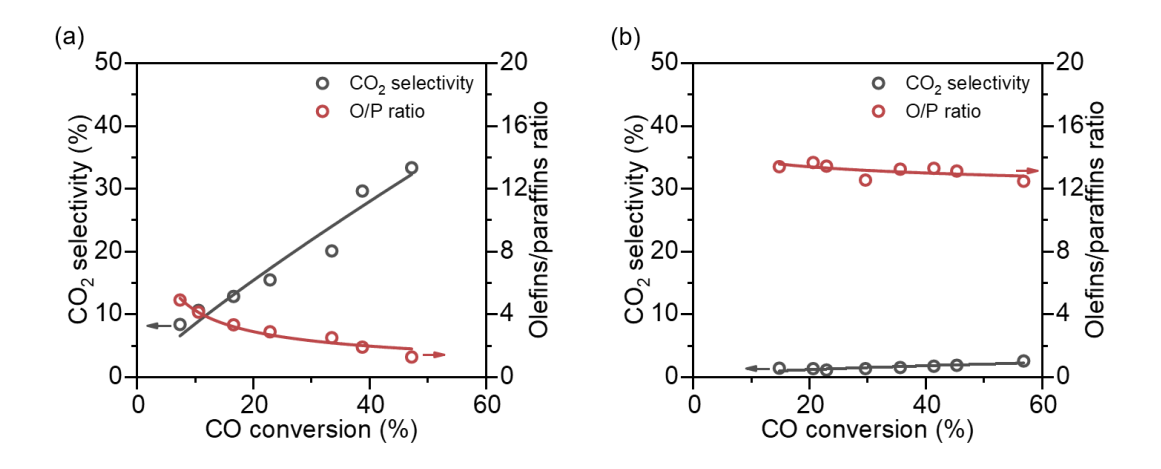


Fig. S11.

CO₂ selectivity and o/p ratio versus CO conversion for χ -Fe₅C₂ (a) and χ -Fe₅C₂-Br (b) at 300 °C. Reaction conditions: for χ -Fe₅C₂, P=10 bar, SV = 60000–600000 mL·g_{cat}-1·h⁻¹, H₂/CO = 2; for χ -Fe₅C₂-Br, P=5 bar, SV = 2000–30000 mL·g_{cat}-1·h⁻¹, H₂/CO = 2, co-feeding 20 ppm CH₃Br. Catalysts were pretreated at 280 °C and 1 bar for 6 h, SV = 12000 mL·g_{cat}-1·h⁻¹, H₂/CO = 2 (χ -Fe₅C₂, syngas without CH₃Br; χ -Fe₅C₂-Br, co-feeding 20 ppm CH₃Br). Data for panel (a) is from Fig. S29; data for panel (b) is from Fig. S10.

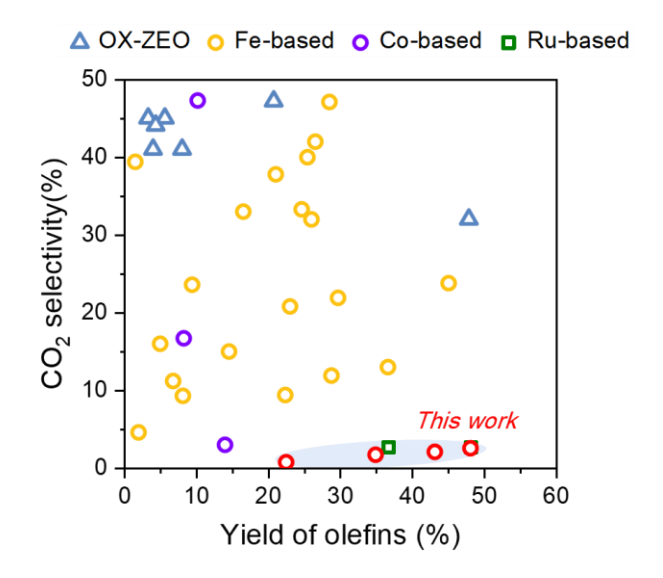


Fig. S12.

Comparison of CO₂ selectivity *vs.* yield of olefins for literature reported OX-ZEO, Fe, Co, and Ru-based catalysts. Red circles are from this work, and the references are listed at Table S8.

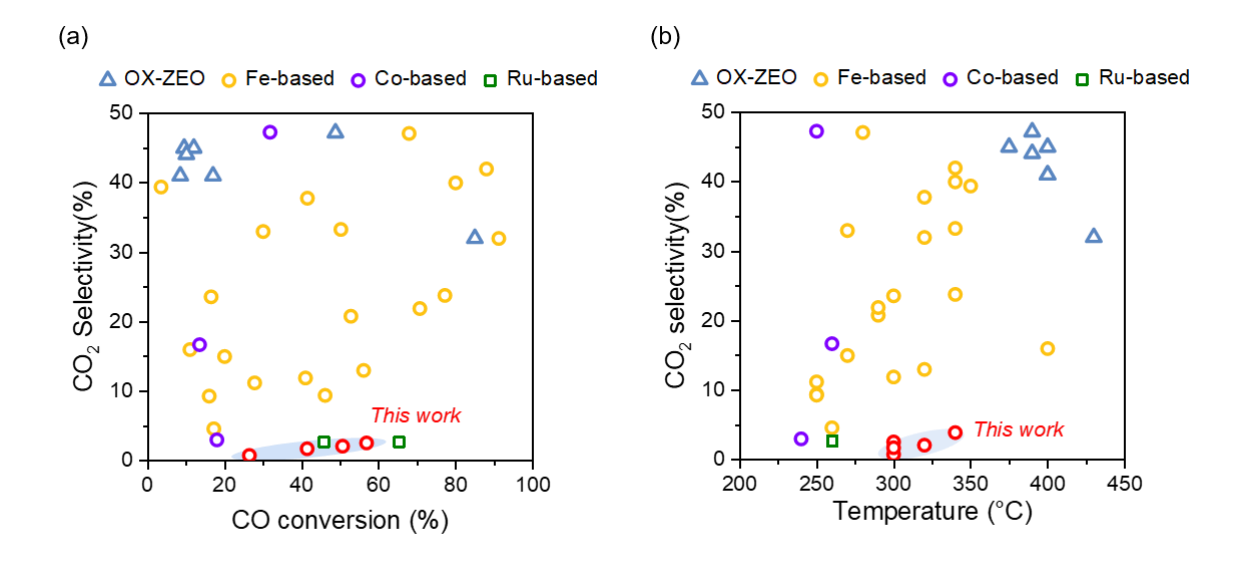


Fig. S13.

Comparison of CO₂ selectivity vs. CO conversion (a) and CO₂ selectivity vs. temperature (b) for literature reported OX-ZEO, Fe, Co, and Ru-based catalysts. Red circles are from this work, and the references are listed at Table S8.

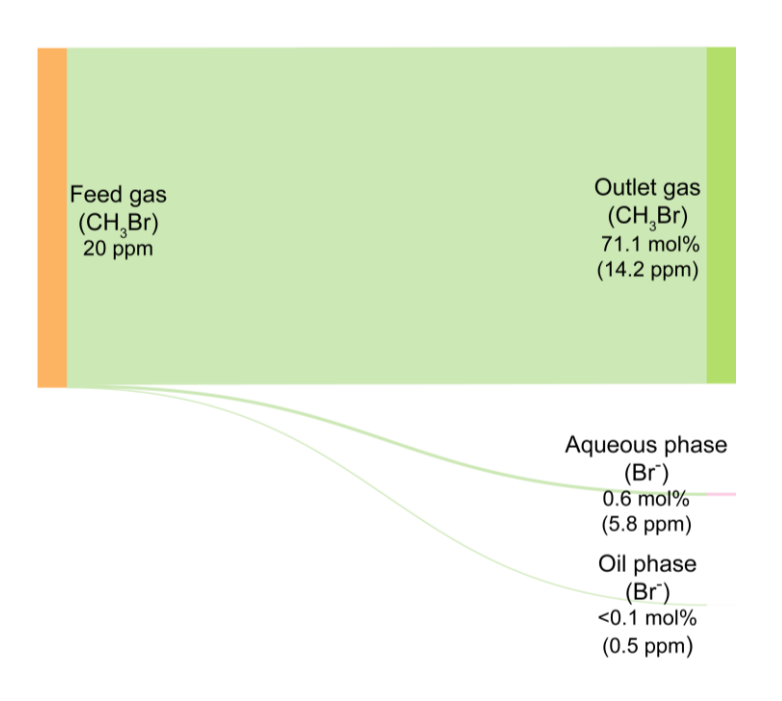


Fig. S14.

Schematic diagram illustrating the fate of bromine from feed gas to effluent streams and products under steady-state FTS reaction conditions. Reaction conditions: 100 mg catalyst, $T = 300 \, ^{\circ}\text{C}$, $P = 10 \, \text{bar}$, $SV = 12000 \, \text{mL} \cdot \text{g}_{\text{cat}}^{-1} \cdot \text{h}^{-1}$, $H_2/\text{CO} = 2$, co-feeding 20 ppm CH₃Br. Catalysts were pretreated at 280 °C and 1 bar for 6 h, $SV = 12000 \, \text{mL} \cdot \text{g}_{\text{cat}}^{-1} \cdot \text{h}^{-1}$, $H_2/\text{CO} = 2$, co-feeding 20 ppm CH₃Br.

Note: Quantitative analysis of Br distribution was conducted by quantifying CH₃Br in the gas phase via mass spectrometry and analyzing Br⁻ in both aqueous and oil phases using ion chromatography. About 71.1 mol% (14.2 ppm) Br remained unreacted in the outlet gas, indicating that most of the Br exited the reaction system in its original form. About 0.6 mol% (5.8 ppm) was detected in the aqueous phase (likely as dissolved HBr), while only a negligible fraction of Br (<0.1mol%) entered the oil phase and Br content was <1 ppm (the results were calculated based on Table S9).

Based on these measurements, a Br mass balance was constructed (Table S10), accounting for ~72% of the total Br inlet. The remaining discrepancy may be attributed to (1) analytical uncertainty at low ppm levels and (2) possible surface-mediated reactions forming minor Br-

containing species that are difficult to detect. This result demonstrates the high gas-phase mobility of Br and confirms that CH₃Br co-feeding effectively modulates catalytic performance without introducing significant impurities into products, highlighting its industrial viability.

Potential challenges associated with co-feeding CH₃Br in industrial practices, notably equipment corrosion and downstream halogen management, can be effectively addressed by adopting well-established technologies from industries experienced in halogen handling (e.g., vinyl chloride and ethylene oxide production). The primary mitigation strategies are as follows:

- 1. Corrosion control: Fixed-bed reactor designs minimize halogen accumulation, while corrosion-resistant linings (e.g., ceramic or Ni–Mo alloys) are used at critical points.
- 2. Halogen removal: (1) Liquid-phase products: water scrubbing followed by sodium-based neutralization and electro-desalting; (2) Gas-phase products: water scrubbing, optionally combined with alkaline or alcohol additives, effectively removes residual CH₃Br. (3) Wastewater: dissolved halide ions are removed using ion-exchange resins.

These described solutions are technologically mature, readily scalable, and necessitate only modest additional investment. These attributes confirm their compatibility with the low-emission FTS installations envisioned for the future of carbon-efficient fuel and chemical manufacturing.

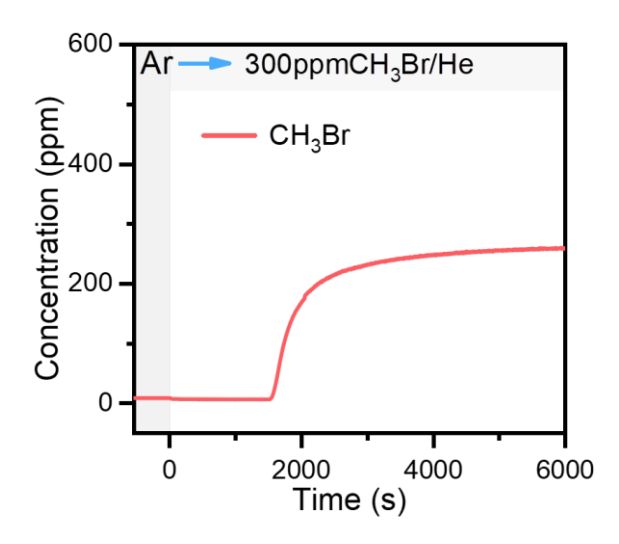


Fig. S15. CH₃Br adsorption-reaction profile on pristine χ -Fe₅C₂ catalyst monitored by mass spectrometer under transient conditions. Reaction condition: 200 mg catalyst, T = 300 °C, P = 1 bar, 50 mL/min Ar switched to He with co-feeding 300 ppm CH₃Br.

Note: The catalyst was initially purged with Ar, followed by exposure to 300 ppm CH₃Br/He at 300 °C. Initially, CH₃Br was nearly completely consumed. Then, a gradual increase and subsequent saturation in CH₃Br concentration reflects the dynamic adsorption and reaction equilibrium on the surface of χ -Fe₅C₂.

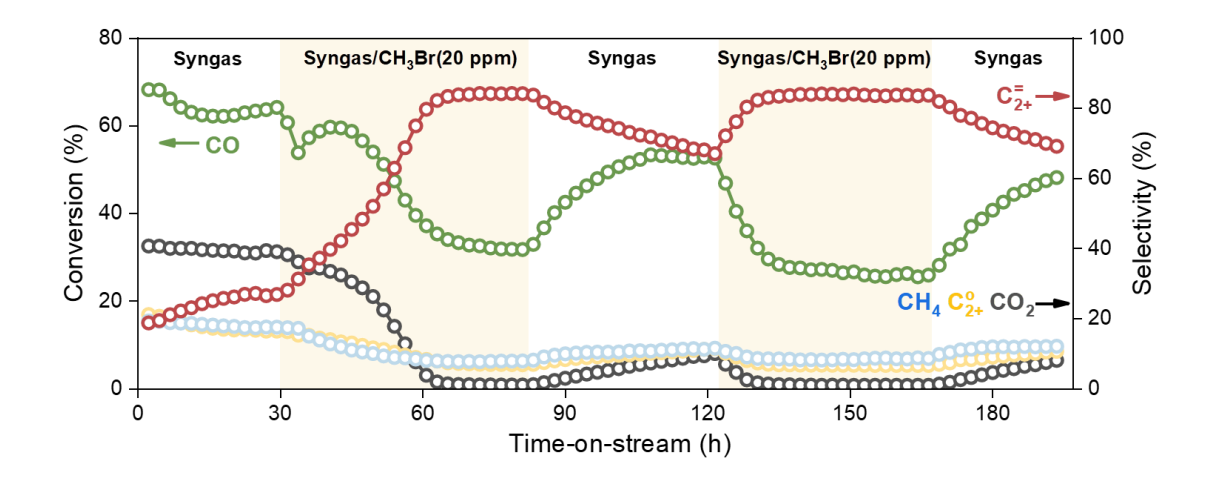


Fig. S16.

CO conversion and product selectivity of Fischer-Tropsch synthesis as a function of time over χ -Fe₅C₂ catalyst. Experiment cycles between syngas without CH₃Br and syngas with 20 ppm CH₃Br. Reaction conditions: 100 mg catalyst, T = 300 °C, P = 10 bar, SV = 12000 mL·g_{cat}⁻¹·h⁻¹, H₂/CO = 2. Catalysts were pretreated at 280 °C and 1 bar for 6 h, SV = 12000 mL·g_{cat}⁻¹·h⁻¹, H₂/CO = 2.

Note: Upon co-feeding 20 ppm CH₃Br into syngas, the FTS performance of the χ-Fe₅C₂ catalyst exhibited a significant change. Within approximately 30 h of co-feeding 20 ppm CH₃Br, the catalyst reached steady state, with CO₂ selectivity dropping sharply from ~30% to ~1%, while the C₂₊ olefin selectivity increased from ~21% to 83%. When CH₃Br co-feeding was removed, CO₂ selectivity gradually increased, accompanied by a progressive decrease in olefin selectivity. Remarkably, co-feeding CH₃Br restored the catalytic performance, demonstrating excellent reversibility. These results highlight the substantial impact of CH₃Br on the FTS reaction network, effectively suppressing CO₂ formation while enhancing the selectivity toward high-value olefins. The catalytic performance changes after CH₃Br removal are attributed to the gradual depletion of surface-bound bromine species. In conclusion, CH₃Br co-

feeding provides an efficient strategy for modulating the catalytic behavior of χ -Fe₅C₂, simultaneously inhibiting CO₂ generation and mitigating olefin over hydrogenation.

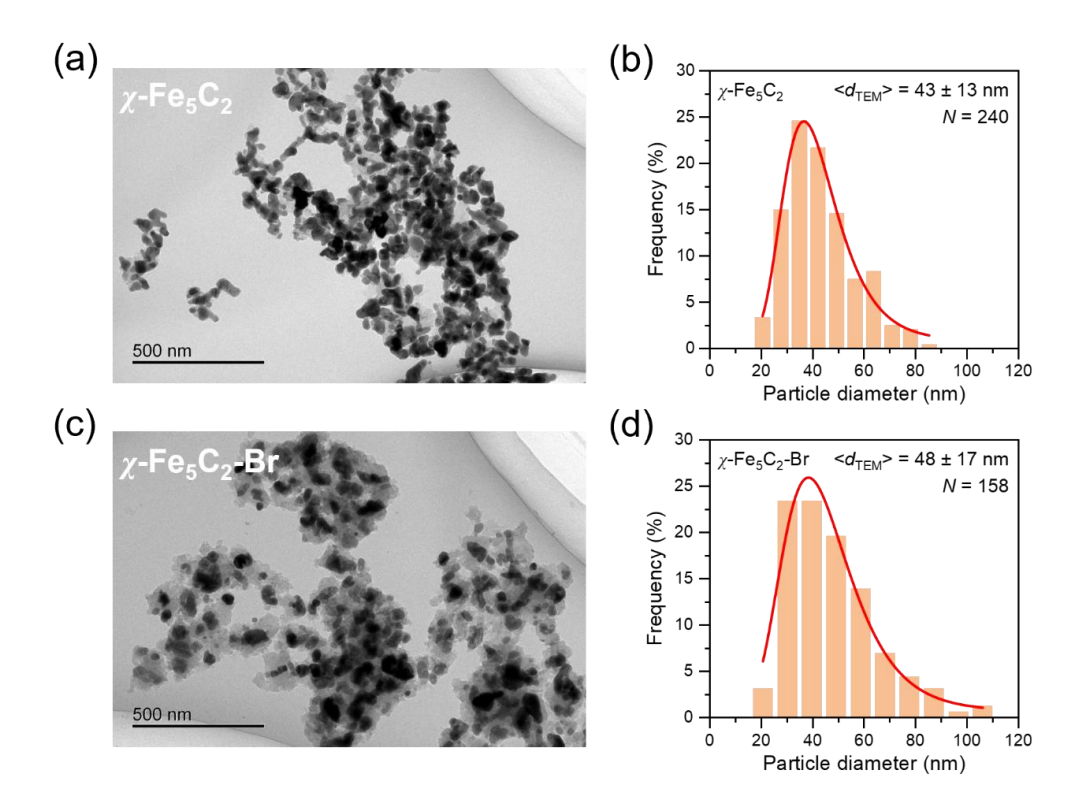
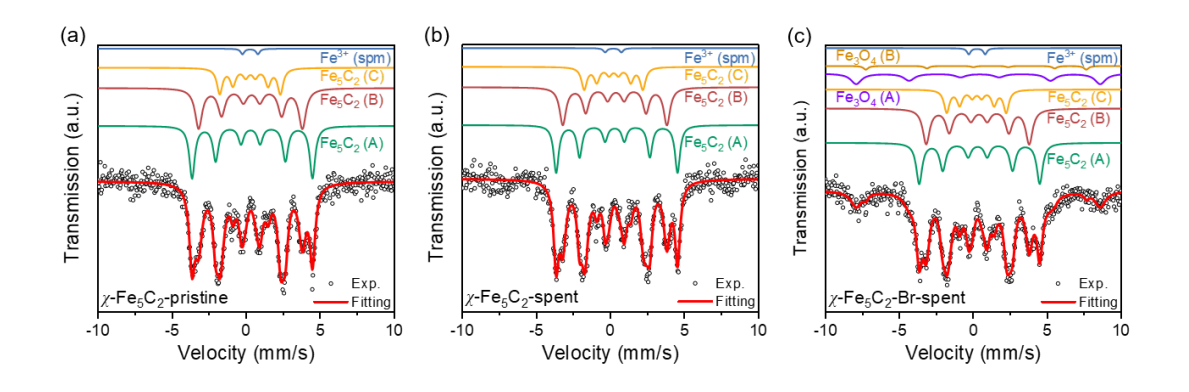


Fig. S17.

TEM characterization of χ -Fe₅C₂-spent (a) and χ -Fe₅C₂-Br-spent (c) catalysts and the distribution of particle sizes of χ -Fe₅C₂-spent (b) and χ -Fe₅C₂-Br-spent (d) catalysts. Reaction conditions: 100 mg catalyst, T = 300 °C, P = 10 bar, SV = 12000 mL·g_{cat}-1·h⁻¹, H₂/CO = 2. χ -Fe₅C₂, syngas without CH₃Br. χ -Fe₅C₂-Br, co-feeding 20 ppm CH₃Br. Catalysts were pretreated at 280 °C and 1 bar for 6 h, SV = 12000 mL·g_{cat}-1·h⁻¹, H₂/CO = 2 (χ -Fe₅C₂, syngas; χ -Fe₅C₂-Br, co-feeding 20 ppm CH₃Br).



Mössbauer spectra of χ -Fe₅C₂-pristine (a), χ -Fe₅C₂-spent (b) and χ -Fe₅C₂-Br-spent (c) catalysts. Reaction conditions: 100 mg catalyst, T = 300 °C, P = 10 bar, SV = 12000 mL·g_{cat}-1·h⁻¹, H₂/CO = 2. χ -Fe₅C₂, syngas without CH₃Br. χ -Fe₅C₂-Br, co-feeding 20 ppm CH₃Br. Catalysts were pretreated at 280 °C and 1 bar for 6 h, SV = 12000 mL·g_{cat}-1·h⁻¹, H₂/CO = 2 (χ -Fe₅C₂, syngas without CH₃Br; χ -Fe₅C₂-Br, co-feeding 20 ppm CH₃Br).

Fig. S18.

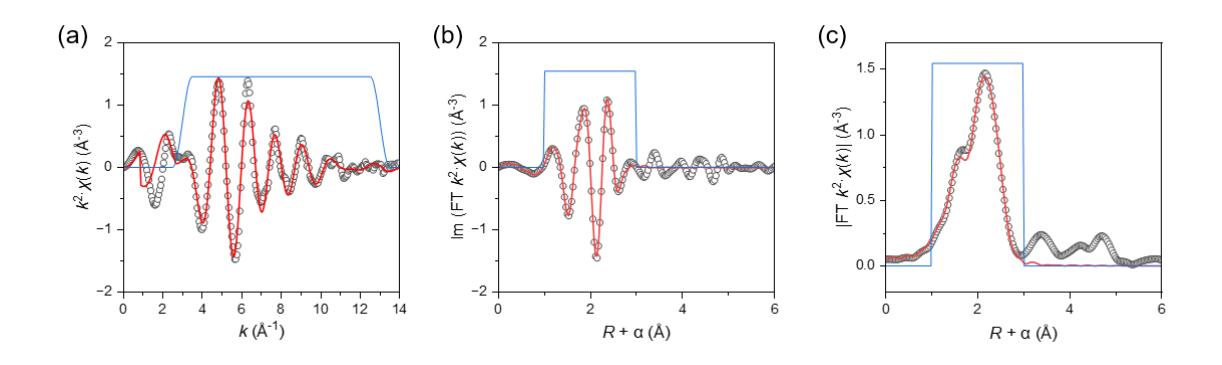


Fig. S19.

Curve-fit (red line) of Fe *K*-edge EXAFS (black dot) for χ -Fe₅C₂-pristine catalyst, shown in *k*-space (a), *R*-space imaginary part (b), and *R*-space (c); the blue line is the fitting windows. The data are k^2 -weighted without phase correction. Catalysts were pretreated at 280 °C and 1 bar for 6 h, SV of 12000 mL·g_{cat}⁻¹·h⁻¹, H₂/CO = 2.

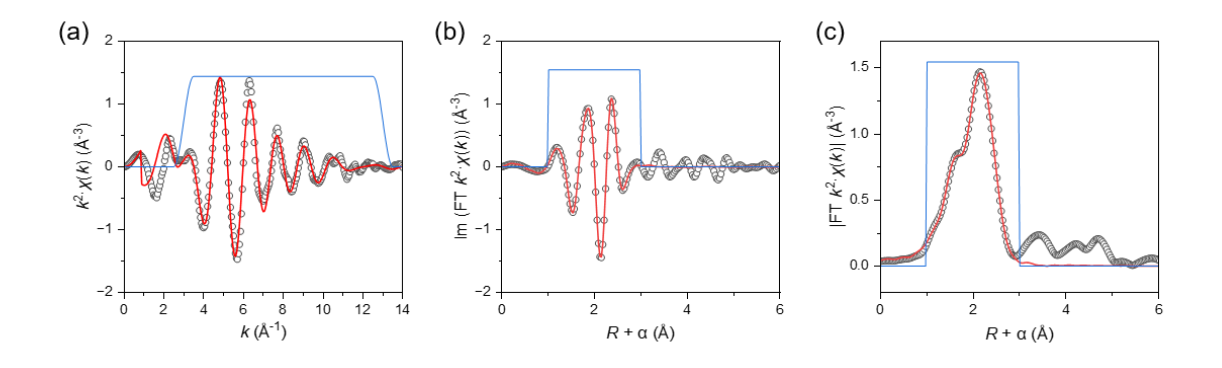


Fig. S20.

Curve-fit (red line) of Fe *K*-edge EXAFS (black dot) for χ -Fe₅C₂-spent catalyst, shown in *k*-space (a), *R*-space imaginary part (b) and *R*-space (c); the blue line is the fitting windows. The data are k^2 -weighted without phase correction. Reaction conditions: 100 mg catalyst, $T = 300 \, ^{\circ}$ C, $P = 10 \, \text{bar}$, SV = 12000 mL·g_{cat}-1·h⁻¹, H₂/CO = 2. Catalysts were pretreated at 280 °C and 1 bar, 6 h, SV of 12000 mL·g_{cat}-1·h⁻¹, H₂/CO = 2.

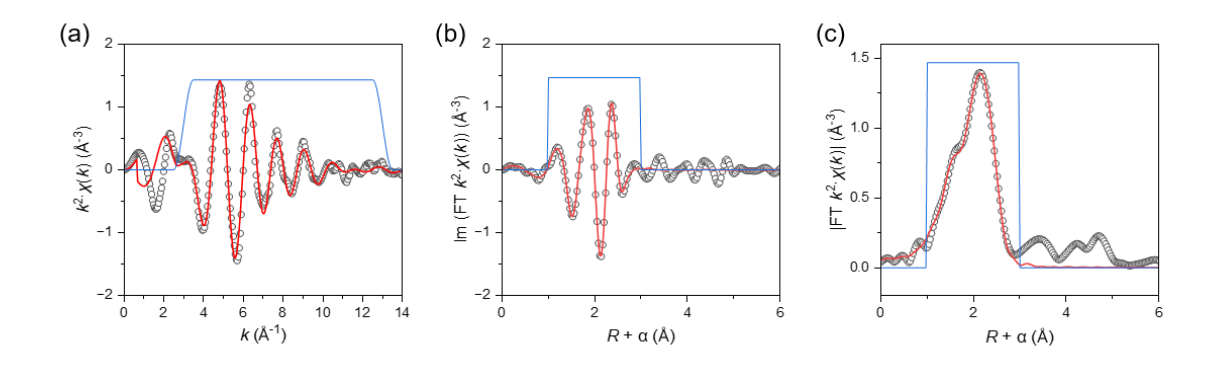


Fig. S21.

Curve-fit (red line) of Fe *K*-edge EXAFS (black dot) for χ -Fe₅C₂-Br-spent catalyst, shown in *k*-space (a), *R*-space imaginary part (b), and *R*-space (c); the blue line is the fitting windows. The data are k^2 -weighted without phase correction. Reaction conditions: 100 mg catalyst, $T = 300 \, ^{\circ}$ C, $P = 10 \, \text{bar}$, SV = 12000 mL·g_{cat}-1·h-1, H₂/CO = 2, co-feeding 20 ppm CH₃Br. Catalysts were pretreated at 280 $^{\circ}$ C and 1 bar for 6 h, SV = 12000 mL·g_{cat}-1·h-1, H₂/CO = 2, co-feeding 20 ppm CH₃Br.

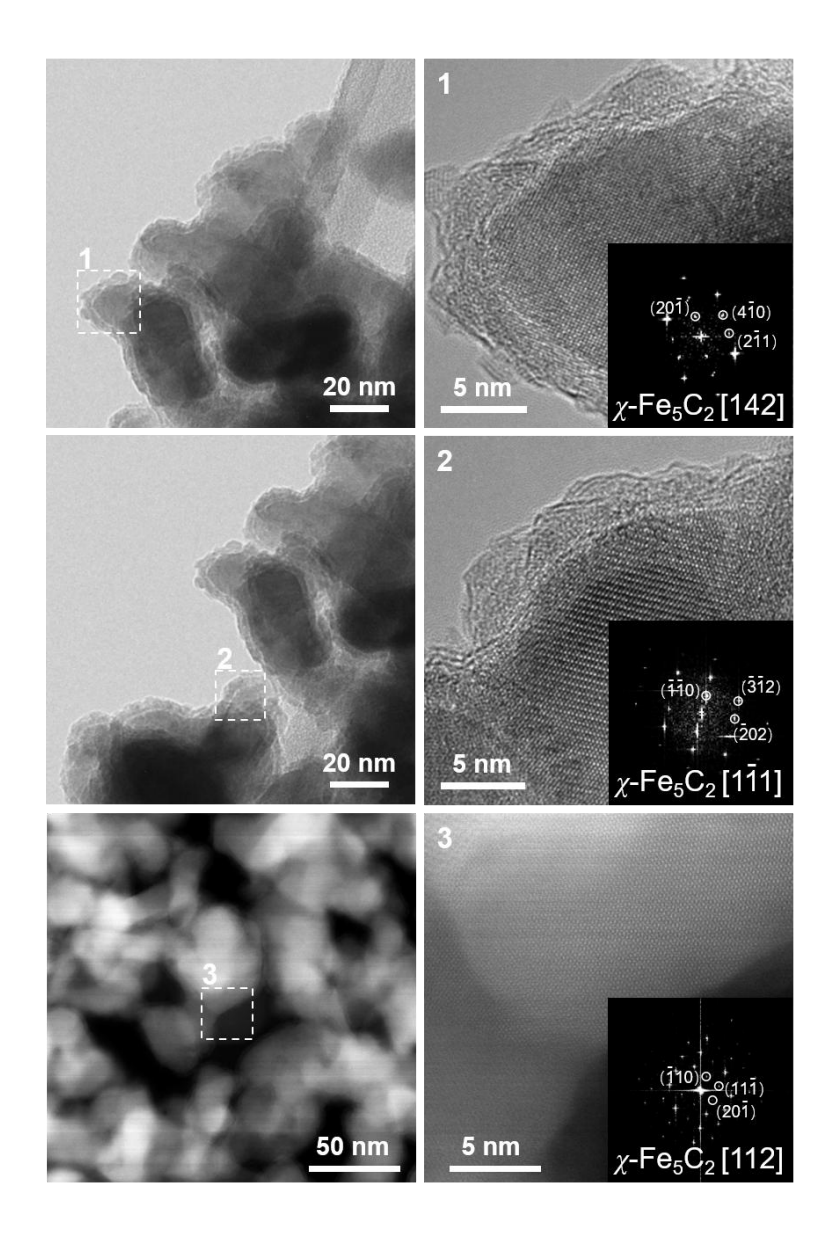


Fig. S22.

TEM, STEM, and corresponding FFT images of pristine χ -Fe₅C₂ catalyst. Figures on the right are magnified images of the corresponding areas selected by dashed squares, with their respective fast Fourier transform (FFT) patterns shown as insets. Catalysts were pretreated at 280 °C and 1 bar for 6 h, SV = 12000 mL·g_{cat}-1·h-1, H₂/CO = 2.

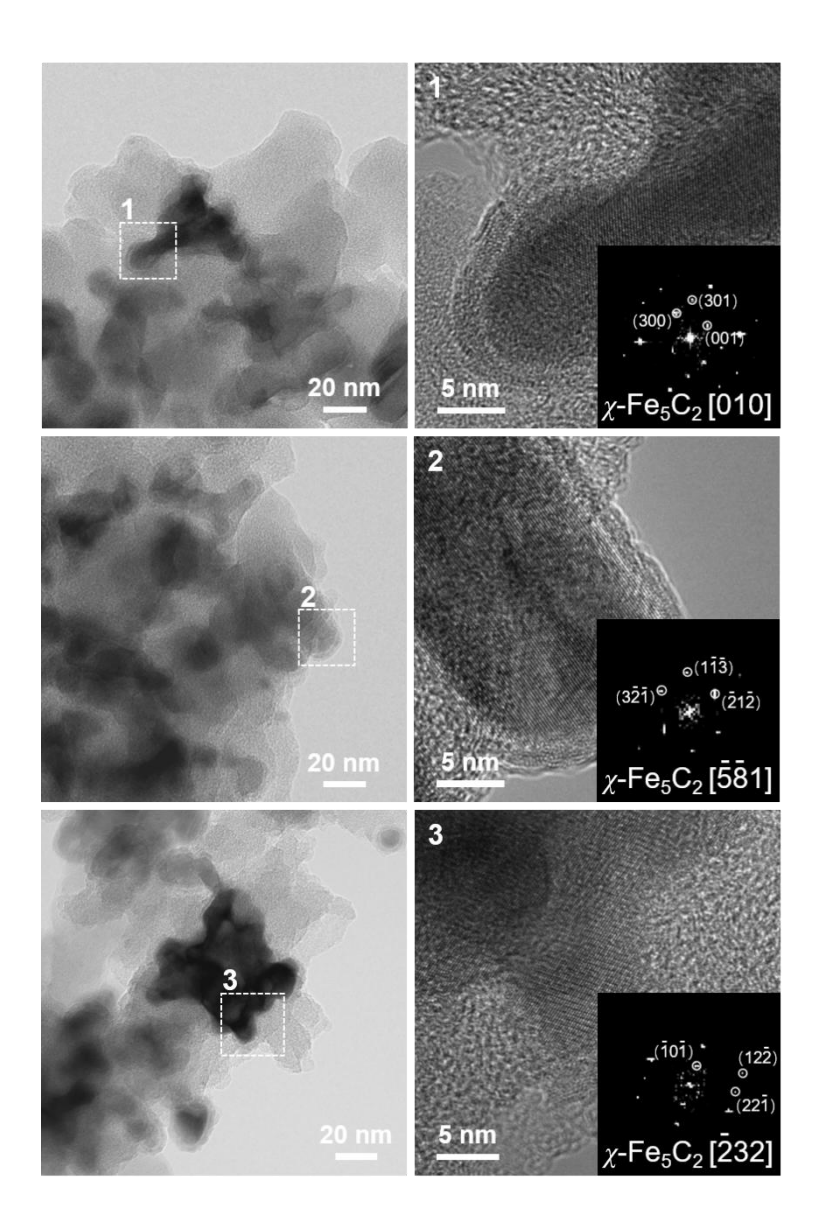


Fig. S23.

TEM and corresponding FFT images of spent χ -Fe₅C₂ catalyst. Figures on the right are magnified images of the corresponding areas selected by dashed squares, with their respective fast Fourier transform (FFT) patterns shown as insets. Reaction conditions: 100 mg catalyst, T = 300 °C, P = 10 bar, SV = 12000 mL·g_{cat}-1·h-1, H₂/CO = 2. Catalysts were pretreated at 280 °C and 1 bar for 6 h, SV = 12000 mL·g_{cat}-1·h-1, H₂/CO = 2.

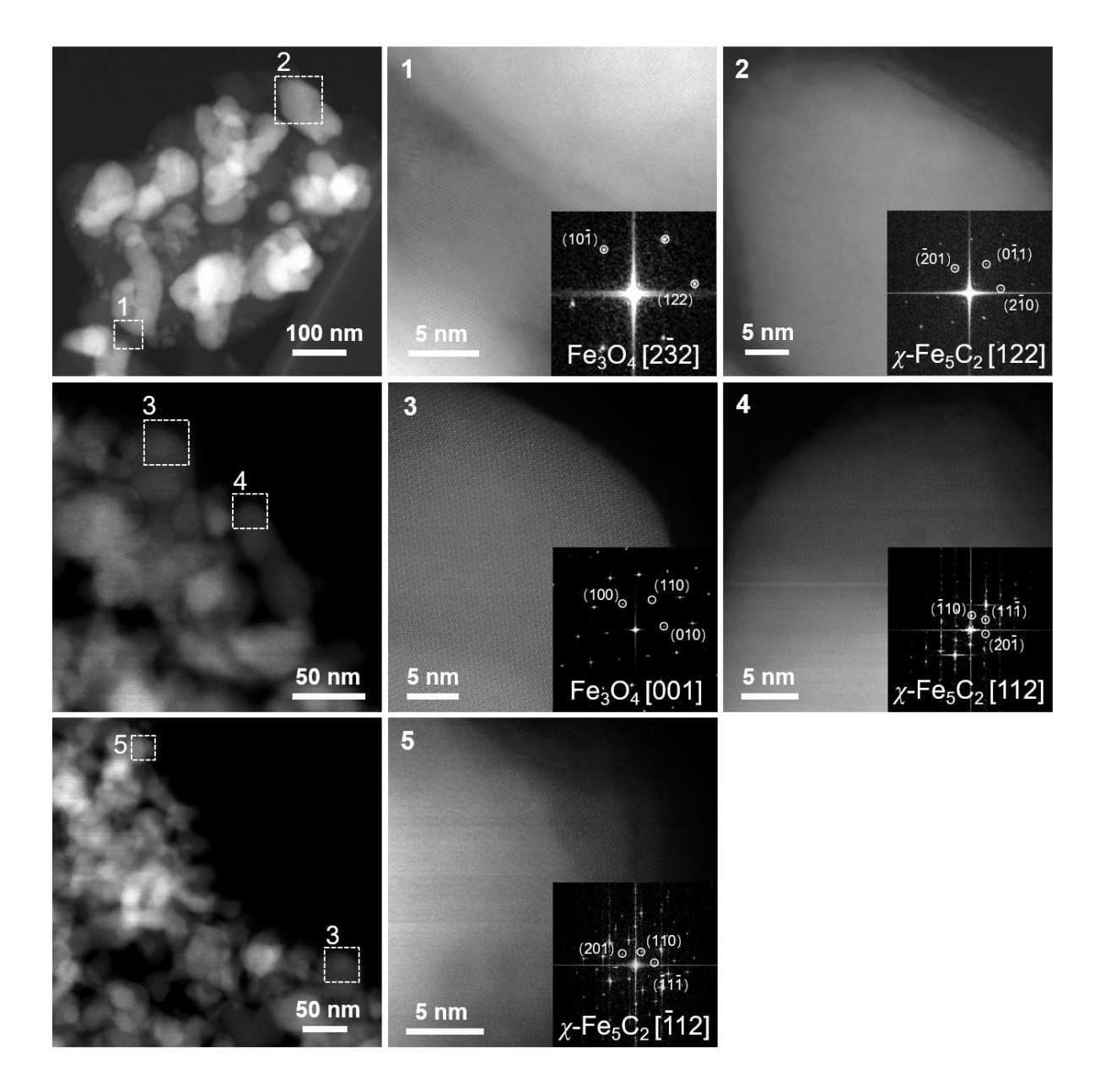


Fig. S24.

STEM and corresponding FFT images of spent χ -Fe₅C₂-Br catalyst. Figures on the right are magnified images of the corresponding areas selected by dashed squares, with their respective fast Fourier transform (FFT) patterns shown as insets. Reaction conditions: 100 mg catalyst, $T = 300 \, ^{\circ}\text{C}$, $P = 10 \, \text{bar}$, SV = 12000 mL·g_{cat}-1·h⁻¹, H₂/CO = 2, co-feeding 20 ppm CH₃Br. Catalysts were pretreated at 280 °C and 1 bar for 6 h, SV = 12000 mL·g_{cat}-1·h⁻¹, H₂/CO = 2, co-feeding 20 ppm CH₃Br.

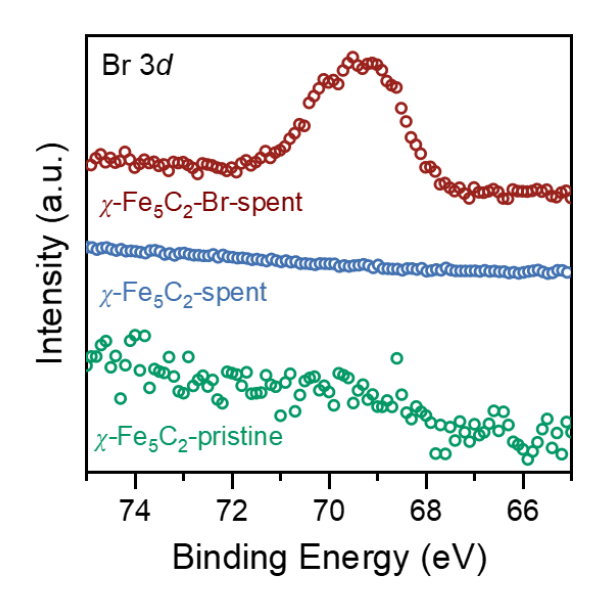


Fig. S25.

Br 3d XPS of χ -Fe₅C₂-pristine, χ -Fe₅C₂-spent, and χ -Fe₅C₂-Br-spent. Both pristine and spent samples were transferred into a UHV chamber without exposure to air. Reaction conditions: 100 mg catalyst, T = 300 °C, P = 10 bar, $SV = 12000 \text{ mL} \cdot \text{g}_{\text{cat}}^{-1} \cdot \text{h}^{-1}$, $H_2/\text{CO} = 2$. χ -Fe₅C₂, syngas without CH₃Br; χ -Fe₅C₂-Br, co-feeding 20 ppm CH₃Br. Catalysts were pretreated at 280 °C and 1 bar for 6 h, $SV = 12000 \text{ mL} \cdot \text{g}_{\text{cat}}^{-1} \cdot \text{h}^{-1}$, $H_2/\text{CO} = 2$ (χ -Fe₅C₂, syngas without CH₃Br; χ -Fe₅C₂-Br, co-feeding 20 ppm CH₃Br).

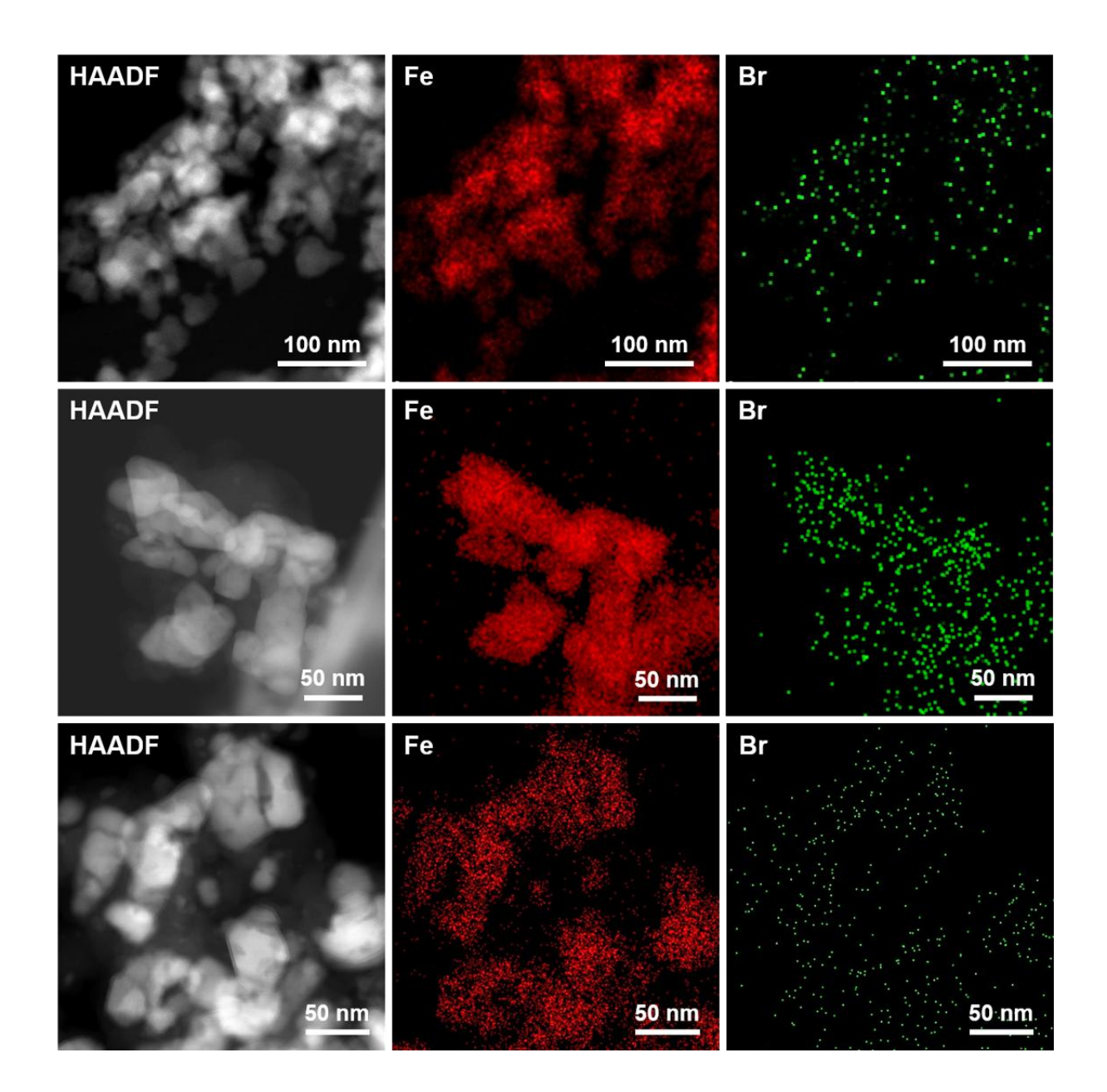
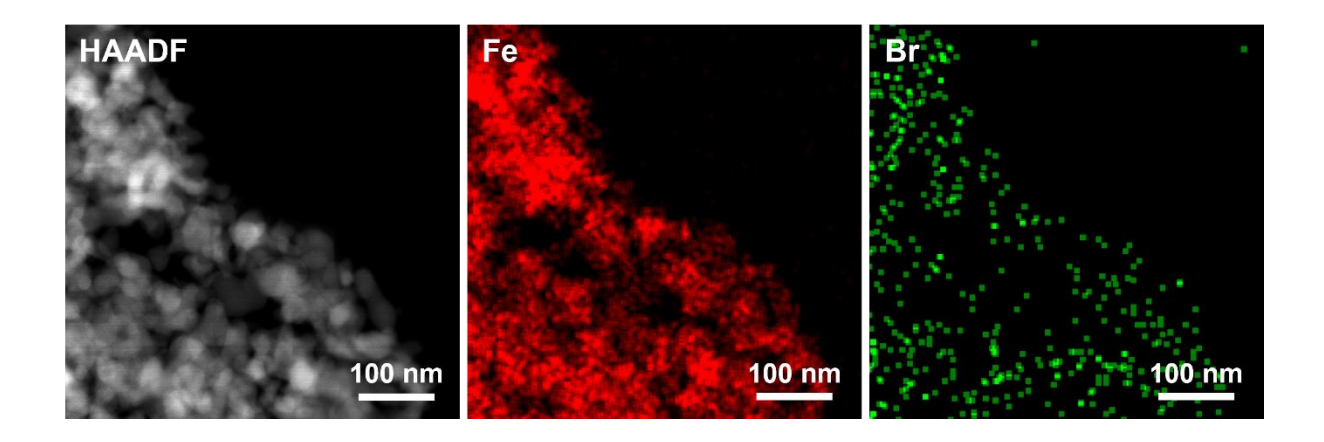


Fig. S26.

STEM and EDS mapping of spent χ -Fe₅C₂-Br catalyst. Reaction conditions: 100 mg catalyst, T = 300 °C, P = 5 bar, SV = 12000 mL·g_{cat}-1·h⁻¹, H₂/CO = 2, co-feeding 20 ppm CH₃Br. Catalysts were pretreated at 280 °C and 1 bar for 6 h, SV = 12000 mL·g_{cat}-1·h⁻¹, H₂/CO = 2, co-feeding 20 ppm CH₃Br.



STEM and EDS mapping of spent χ -Fe₅C₂-Br catalyst. Reaction conditions: 100 mg catalyst, T = 300 °C, P = 10 bar, SV = 12000 mL·g_{cat}-¹·h-¹, H₂/CO = 2, co-feeding 20 ppm CH₃Br. Catalysts were pretreated at 280 °C and 1 bar for 6 h, SV = 12000 mL·g_{cat}-¹·h-¹, H₂/CO = 2, co-feeding 20 ppm CH₃Br.

Fig. S27.

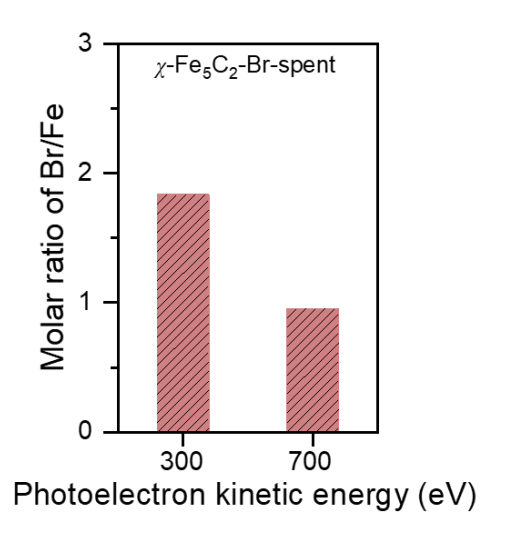


Fig. S28.

Synchrotron XPS result of χ -Fe₅C₂-Br-spent catalyst. The molar ratio of Br/Fe was calculated by the integration of XPS peaks of Br 3d and Fe 2p. Reaction conditions: 100 mg catalyst, T = 300 °C, P = 10 bar, SV = 12000 mL·g_{cat}-1·h⁻¹, H₂/CO = 2, co-feeding 20 ppm CH₃Br. Catalysts were pretreated at 280 °C and 1 bar for 6 h, SV = 12000 mL·g_{cat}-1·h⁻¹, H₂/CO = 2, co-feeding 20 ppm CH₃Br.

Note: Detecting photoelectrons with different energies in synchrotron XPS can probe the chemical state of target element at different depths of a material. The probing depth is governed by the inelastic mean free path (IMFP) of the emitted photoelectrons, which is a function of their kinetic energy. Photoelectrons with lower kinetic energy have a shorter IMFP and are thus more surface-sensitive, whereas those with higher kinetic energy possess a longer IMFP, providing information from deeper within the bulk of the material.

In this experiment, the Br/Fe molar ratio derived from the more surface-sensitive 300 eV photoelectrons was significantly higher than that from the more bulk-sensitive 700 eV photoelectrons. Since the catalyst's main component is χ -Fe₅C₂, which has a well-defined crystal structure, this result provides evidence that Br is enriched on the surface of the crystalline χ -Fe₅C₂.

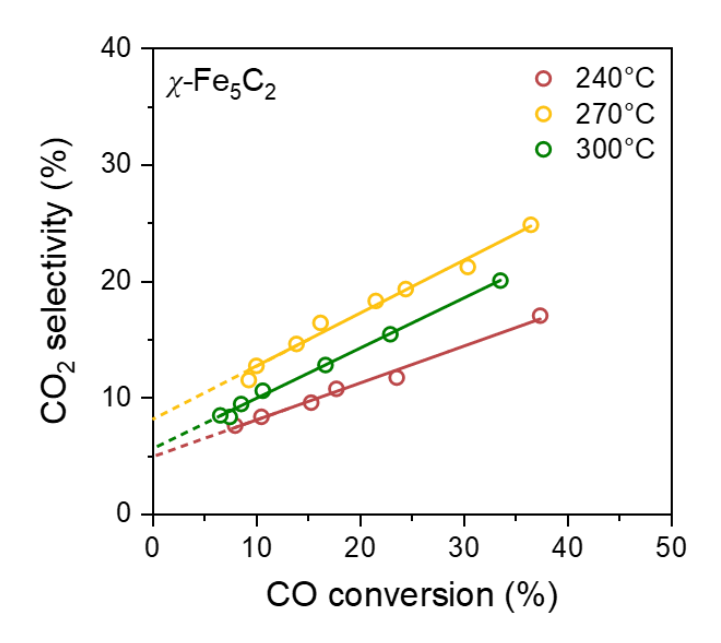


Fig. S29. CO conversion vs. CO₂ selectivity for the χ -Fe₅C₂ catalyst at 240, 270, and 300 °C. Reaction conditions: 100 mg catalyst, P=10 bar, SV = 12000–600000 mL·g_{cat}-1·h⁻¹; H₂/CO = 2. Catalysts were pretreated at 280 °C and 1 bar for 6 h, SV = 12000 mL·g_{cat}-1·h⁻¹, H₂/CO = 2.

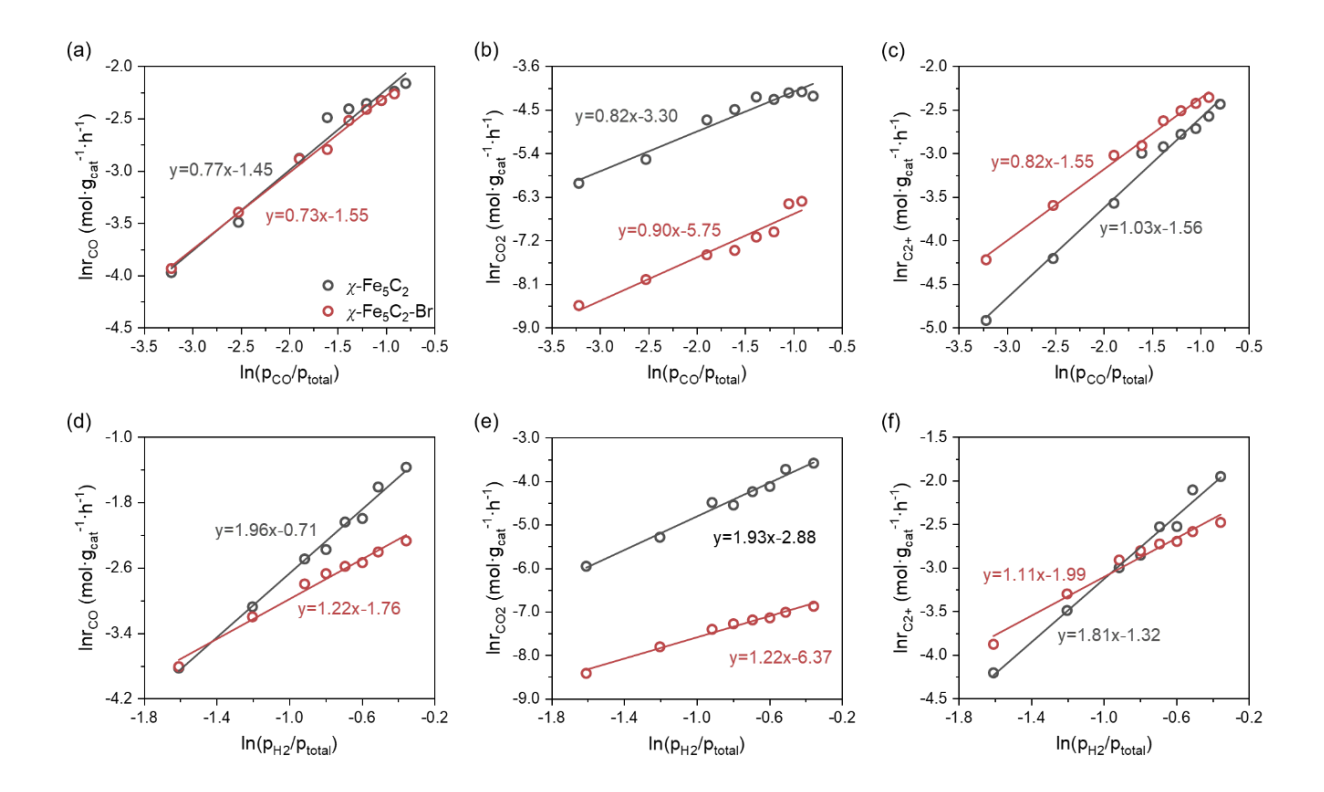


Fig. S30.

Kinetic analyses of Fischer-Tropsch synthesis and CO₂ formation over χ -Fe₅C₂ and χ -Fe₅C₂-Br catalysts. (a–c) Dependence of CO consumption rate (a), CO₂ formation rate (b), and C₂₊ hydrocarbon formation rate (c) on the partial pressure of CO ($p_{\text{CO}}/p_{\text{total}}$). (d–f) Dependence of CO consumption rate (d), CO₂ formation rate (e), and C₂₊ hydrocarbon formation rate (f) on the partial pressure of H₂ ($p_{\text{H2}}/p_{\text{total}}$). Linear fits yield reaction orders as slopes. Reaction conditions: T = 300 °C, P = 10 bar, balanced by Ar, SV = 50000 – 160000 (for χ -Fe₅C₂) or 30000 - 130000 (for χ -Fe₅C₂-Br) mL·g_{cat}-1·h-1. The CO conversion of χ -Fe₅C₂ and χ -Fe₅C₂-Br catalysts are controlled to be close and was kept lower than 10-15%.

Note: Preliminary kinetic analysis reveals that co-feeding CH₃Br significantly alters the reaction kinetics on the χ -Fe₅C₂ catalyst. While the reaction order with respect to CO remains largely unchanged, the reaction order for H₂ decreases substantially in the presence of bromine—from approximately 2.0 to 1.2 for CO consumption and from 1.8 to 1.1 for C₂₊ formation. This effect suggests that adsorbed bromine species may inhibit hydrogen-assisted CO dissociation in FTS. Furthermore, the rate of CO₂ formation is suppressed by two to three

orders of magnitude. This observation is consistent with bromine-induced site blocking, which effectively shuts down the WGS and Boudouard reaction pathways.

While these trends offer valuable insights, the inherent complexity of the FTS reaction network makes a rigorous quantitative interpretation challenging. Specifically, because:

- 1. FTS network includes multiple parallel reactions (WGS, Boudouard reaction, CO hydrogenation and chain growth), all sensitive to CO/H₂ ratio, temperature, and water partial pressure. Besides, these parameters can also dynamically alter catalyst states (e.g., degree of carburization).
- 2. Apparent reaction orders reflect contributions from both intrinsic kinetics and surface coverage effects, making it challenging to isolate the influence of Br on a single elementary step.

In summary, this kinetic data provides a qualitative demonstration of the impact of cofeeding CH₃Br, particularly in suppressing CO₂ formation and altering the pathway for Hassisted CO activation. Given the complexities outlined above, the development of a detailed, quantitative kinetic model is beyond the scope of the present work.

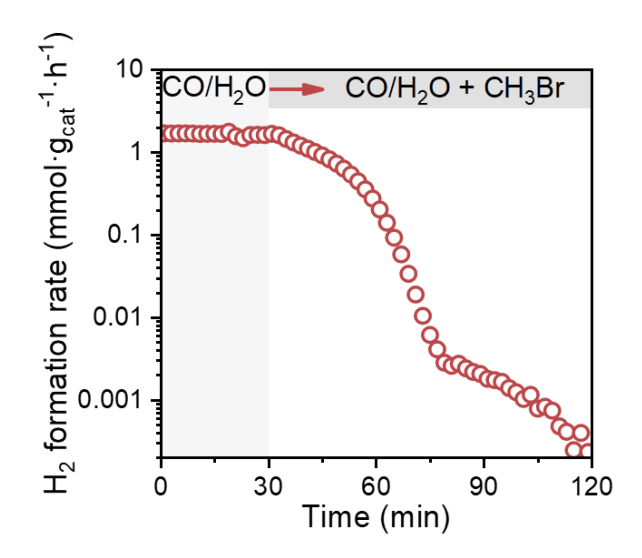


Fig. S31. Effect of CH₃Br co-feeding on H₂ formation rates in water-gas shift reaction over Fe₃O₄ catalyst. Reaction conditions: 50 mg catalyst, T = 300 °C, P = 1 bar, 10 mL/min CO/H₂O/Ar = 2/2/96 switched to CO/H₂O/Ar = 2/2/96 with co-feeding 300 ppm CH₃Br.

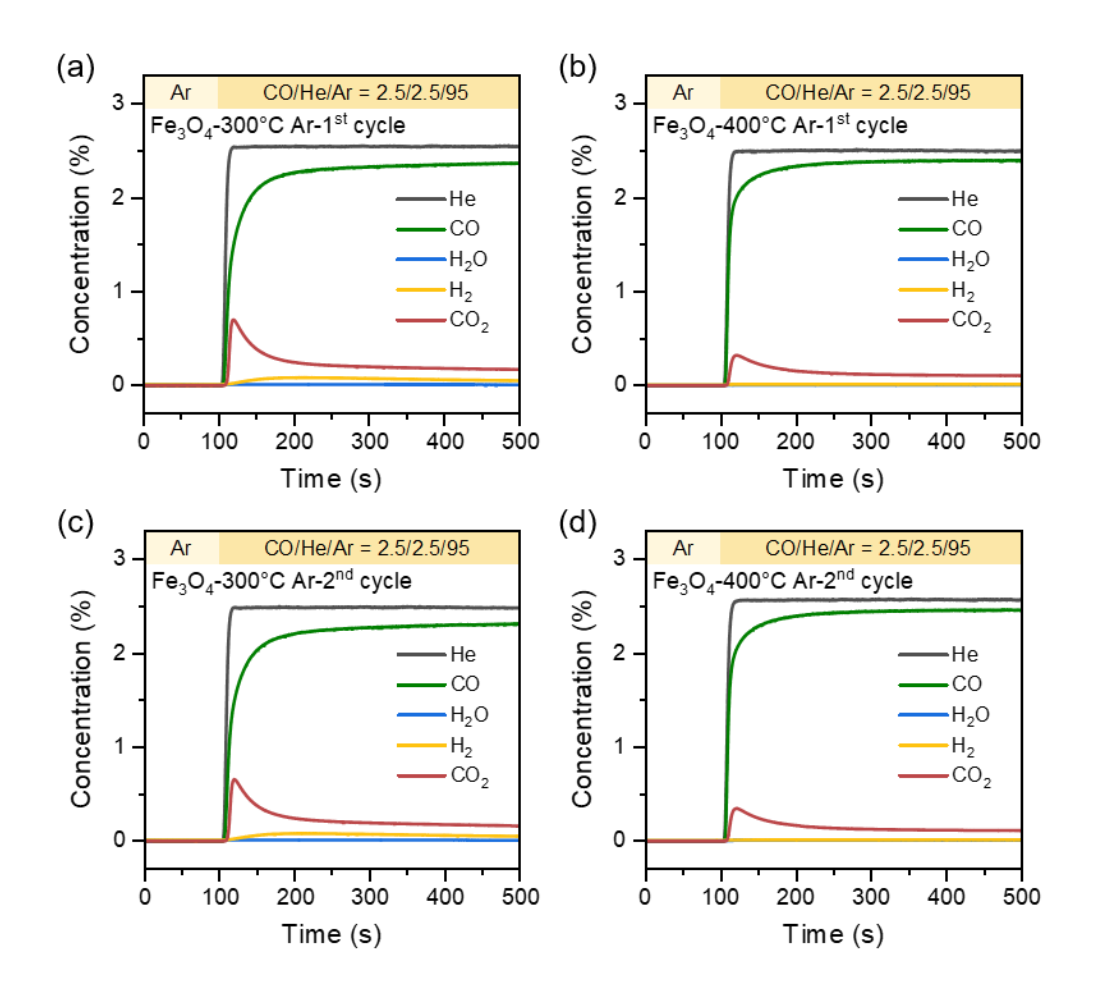
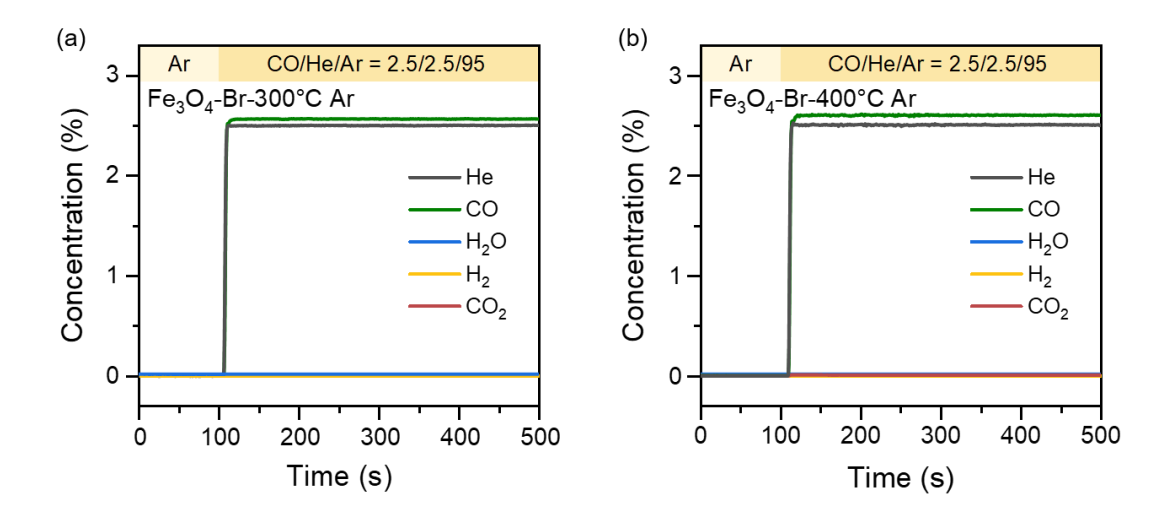


Fig. S32.

Ar \rightarrow CO/He/Ar = 2.5/2.5/95 TKA results of Fe₃O₄ catalysts for the first (a, b) and second cycle (c, d). Each cycle has a process of (1) holding at 300 °C in Ar, then introducing 20 mL/min H₂O/He/Ar = 2.5/2.5/95 for 20 min (treatment in H₂O atmosphere); (2) then catalysts were firstly purged in Ar for 30 min and then treated at 300 °C and 400 °C in Ar for 60 min; (3) then cooling to 300 °C and holding for 10 min; (4), and finally Ar \rightarrow CO/He/Ar = 2.5/2.5/95 at 300 °C.

Note: To investigate the role of surface hydroxyl groups (OH*) in the WGS reaction on Fe₃O₄, a transient kinetic analysis (TKA) experiment was conducted using a gas-switching process (Fig. S32). In each cycle, after H₂O/He/Ar pretreatment, the catalyst was then purged in Ar atmosphere and treated for 60 min at a certain pretreatment temperature (300 °C or 400 °C),

followed by a switch to 20 mL/min CO/He/Ar = 2.5/2.5/95 at 300 °C. Two successive cycles were performed following pretreatment at 300 °C and 400 °C in Ar, respectively. Low temperature (300 °C) pretreatment can retain most of the surface hydroxyl group (OH*), but high temperature (400 °C) pretreatment would dehydrate the surface and reduce the density of surface OH*. The results show that, for sample treated at 300 °C in Ar, rapid CO consumption and a corresponding formation of CO₂ and H₂ were observed immediately after switching to CO/He/Ar, indicating the occurrence of the WGS reaction. Notably, the CO₂ production on catalyst after 400 °C & Ar pretreatment was markedly lower than that observed after 300 °C pretreatment in both cycles, and there was almost no H₂ formation. This suggests that high-temperature pretreatment eliminates the surface OH* and inhibits WGS process, and the surface OH* group is the key species for CO conversion steps in WGS.



Ar \rightarrow CO/He/Ar = 2.5/2.5/95 TKA results of Fe₃O₄-Br catalysts. Reaction conditions: 100 mg catalyst, pretreatment process includes (1) holding at 300 °C in Ar, then introducing 20 mL/min H₂O/He/Ar = 2.5/2.5/95 for 20 min (treatment in H₂O atmosphere); (2) then catalysts were firstly purged in Ar for 30 min and catalysts were treated at 300 °C (a) and 400 °C (b) in Ar for

60 min; (3) then cooling to 300 °C and holding for 10 min; (4) and finally $Ar \rightarrow CO/He/Ar =$

Fig. S33.

2.5/2.5/95 at 300 °C.

Note: For Fe₃O₄-Br catalyst, no CO₂ formation was observed after CO was introduced, regardless of whether the catalyst was pretreated at 300 °C or 400 °C. This suggests Br either blocks the formation of surface hydroxyl group (OH*), or deactivates the surface OH* for the conversion of CO to CO₂.

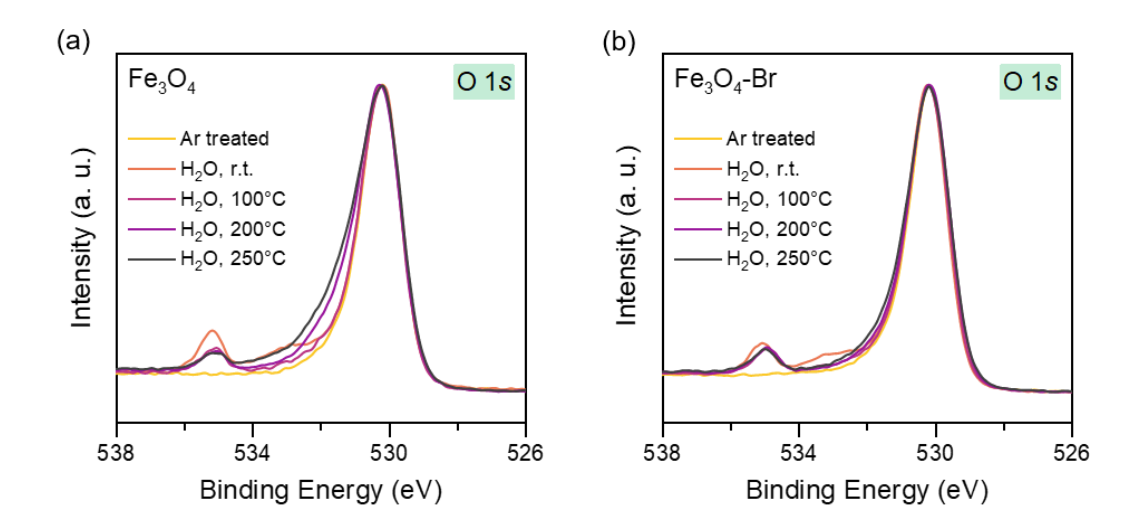


Fig. S34. O 1s XPS of Fe₃O₄ (a) and Fe₃O₄-Br (b) catalysts after pretreatment at 400 °C in Ar and elevating temperature in 1 mbar H₂O from r.t. to 250 °C. Conditions: r.t., 100, 200 and 250 °C, in 1 mbar H₂O atmosphere.

Note: Pretreatment at 400°C in Ar removed most of the surface hydroxyl group (OH*) on Fe₃O₄ (Fig. S32). Subsequently, a temperature ramping in the presence of H₂O would regenerate OH* if the catalyst can dissociate H₂O. For Fe₃O₄, increasing the temperature led to a pronounced enhancement in the O 1*s* signal corresponding to surface hydroxyl group (OH_{ads}) at ~531.5 eV, rising from 10.1% at room temperature to 26.4% at 250 °C (Table S17, Fig. S34 and Fig. S35 (a, b)). This indicates substantial water dissociative adsorption on the Fe₃O₄ surface at elevated temperatures. In sharp contrast, the Fe₃O₄-Br catalyst exhibited a much smaller increase in OH_{ads} signal intensity, with only a modest rise from 9.7% to 13.5% over the same temperature range (Table S18, Fig. S34 and Fig. S35 (c, d)). This observation suggests that Br incorporation remarkably suppresses the dissociation of H₂O and blocks the surface OH* formation on the catalyst. The results verify that the H₂O activation ability on the catalyst decreases after Br modification and provides mechanistic insight to explain the inhibition effect of Br on the WGS reaction over Fe₃O₄ catalyst.

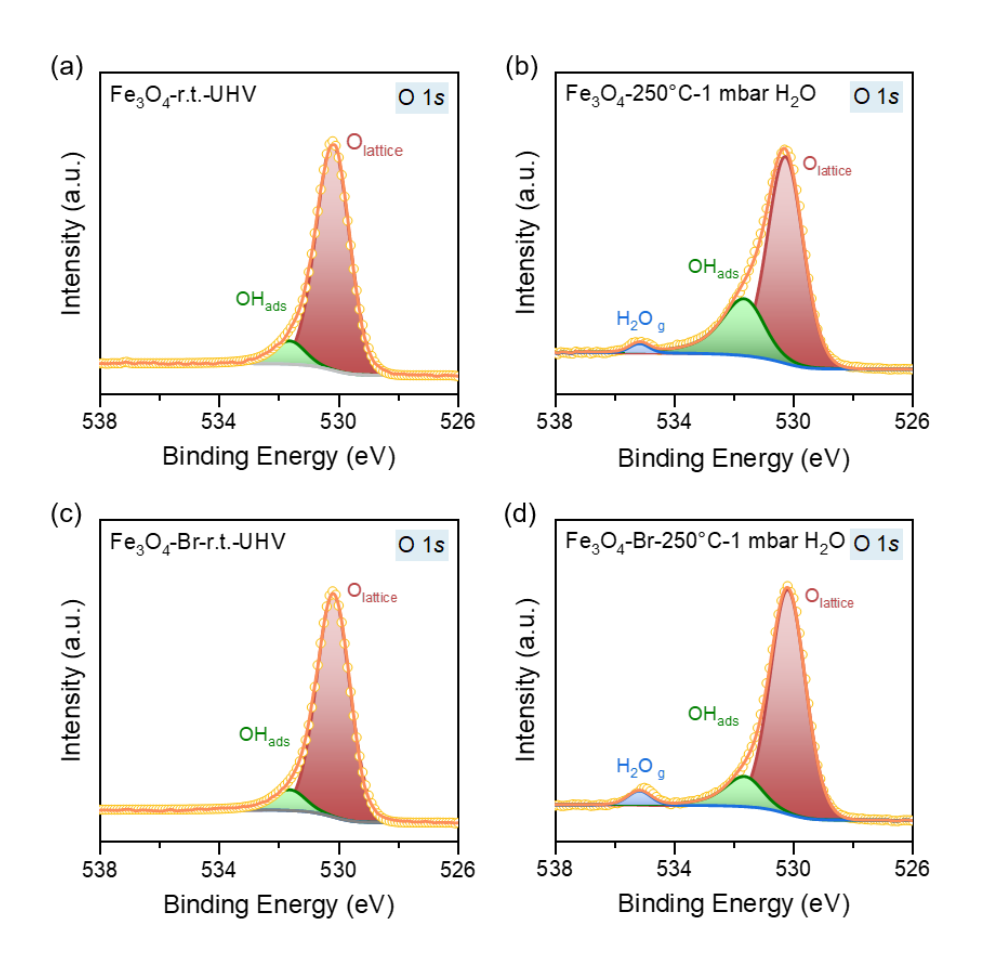


Fig. S35.

Fitting of O 1s XPS of Fe₃O₄ (a, b) and Fe₃O₄-Br (c, d) after 400 °C Ar pretreatment, measured at room temperature under UHV and in 1 mbar H₂O at 250 °C. The fitting parameters were listed in Tables S17 and S18.

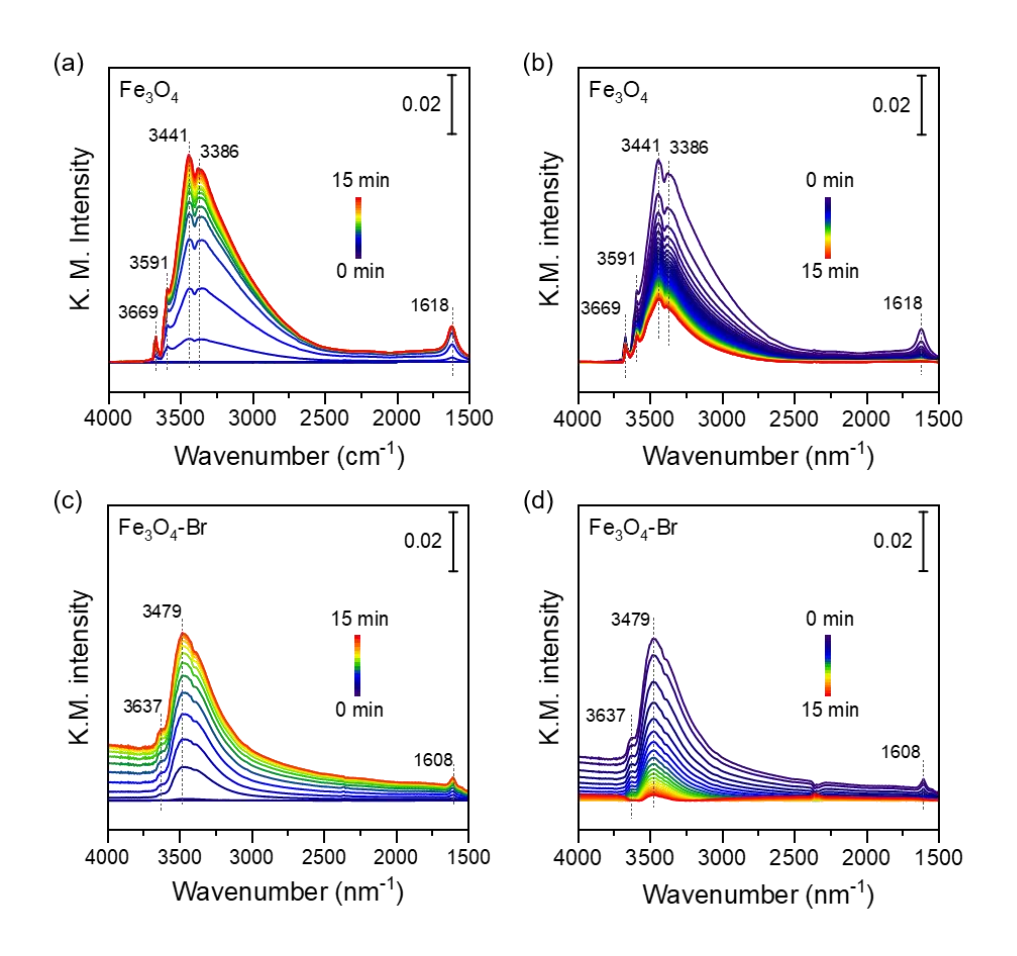


Fig. S36.

Diffuse reflectance infrared Fourier transform spectroscopy (DRIFTS) experiments of Fe₃O₄ (a, b) and Fe₃O₄-Br (c, d) catalysts during H₂O treatment and Ar purging. Reaction conditions: α-Fe₂O₃ catalysts were pretreated at 300 °C with 10 mL/min CO/H₂O/Ar = 0.5/0.5/99 in homemade DRIFTS cell (phase transformation to Fe₃O₄), then switched to 10 mL/min Ar (for Fe₃O₄) or 10 mL/min 500 ppm CH₃Br/He (for Fe₃O₄-Br) for 1 h. After purging for 30 min in Ar, the temperature was elevated to 400 °C and held for 60 min. After that, the sample was cooled to 300 °C and background was collected. Then the gas was switched to 10 mL/min H₂O/Ar = 0.5/99.5 (a, c), held for 15 min until the spectrum remained steady, then switched back to 10 mL/min Ar (b, d).

Note: Pretreatment at 400°C in Ar removed most of the surface hydroxyl group (OH*) on Fe₃O₄ (Fig. S32). Subsequently, H₂O exposure at 300°C would regenerate OH* if the catalyst

can dissociate H₂O. For Fe₃O₄ catalyst, several well-defined peaks were observed in the O-H stretching region (3500–3700 cm⁻¹), including peaks at 3669, 3591, 3441 and 3386 cm⁻¹, which were attributed to surface hydroxyl group (OH*). Additionally, peak at 1618 cm⁻¹ corresponding to the bending vibration band of gaseous H₂O was detected. After introduction of H₂O, then switching and purging with Ar, the surface OH* peaks at 3500–3700 cm⁻¹ persisted over time while gaseous H₂O peak at 1618 cm⁻¹ disappeared, indicating substantial adsorption and dissociation of H₂O on the Fe₃O₄ surface and formation of surface OH*. In contrast, OH* and H₂O species on Fe₃O₄-Br catalyst exhibited distinctly different vibrational characteristics under the same conditions. Although OH* stretching bands at 3479 and 3637 cm⁻¹ were also present, their intensities were nearly negligible. This suggests that the introduction of Br effectively suppresses the formation of OH* groups and H₂O dissociation step on the catalyst surface. Taken together, the DRIFTS results are in good agreement with the XPS results (Figs. S34 and S35, Table S17 and Table S18) and TKA analyses (Figs. S32 and S33), providing compelling evidence that Br inhibits the formation of surface OH* and activation of H₂O molecules on the Fe₃O₄ surface, thereby inhibiting the WGS reaction.

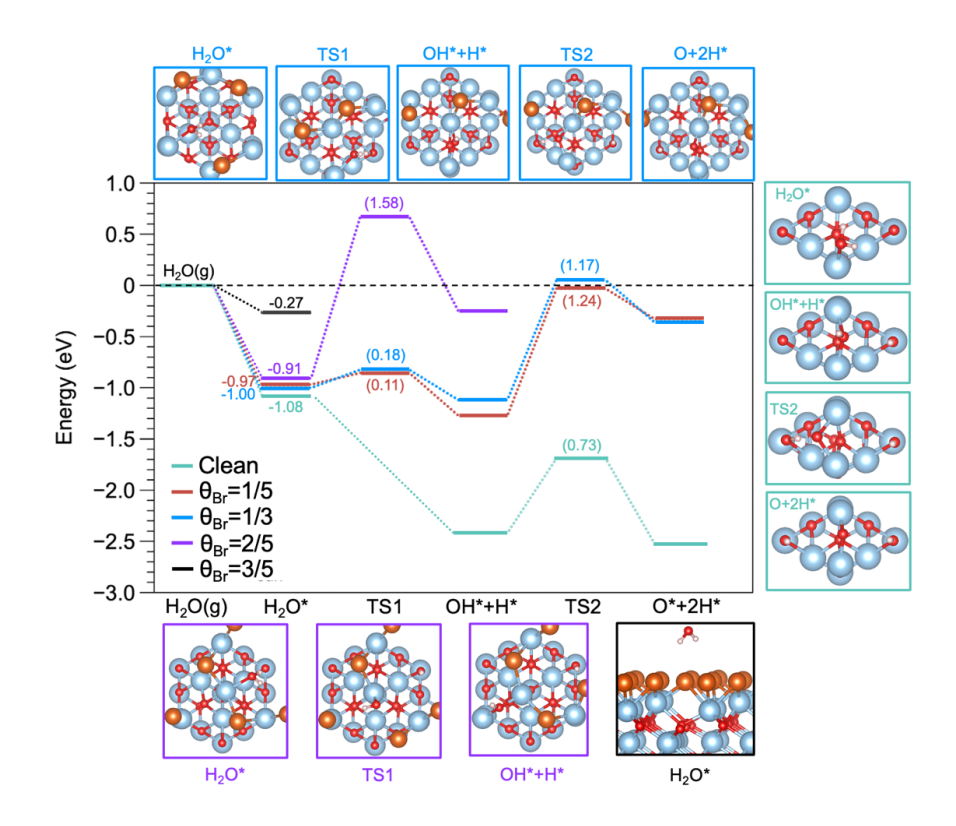


Fig. S37.

DFT-calculated water dissociation reaction energy profiles. Water dissociation pathways on Fe₃O₄ (111) surfaces at different Br coverages ($\theta_{Br} = 0$ –3/5), highlighting significant barrier increases with Br adsorption.

Note: On the clean Fe₃O₄ (111) surface (in the absence of Br), DFT calculations present a barrierless dissociation of H₂O at the first step and a relatively low activation energy of 0.73 eV for the second-step transition state (TS2), indicating a highly favorable H₂O dissociation process. However, the introduction of moderate Br coverage ($\theta_{Br} = 1/5-1/3$) significantly increases both barriers: TS1 rises to 0.11–0.18 eV, and TS2 rises to 1.24 and 1.17 eV, respectively. Further increasing the Br coverage to $\theta_{Br} = 2/5$ results in a dramatic increase in the TS1 barrier to 1.58 eV, which exceeds the desorption energy of molecular H₂O, suggesting that H₂O molecules prefer desorption over dissociation at this coverage.

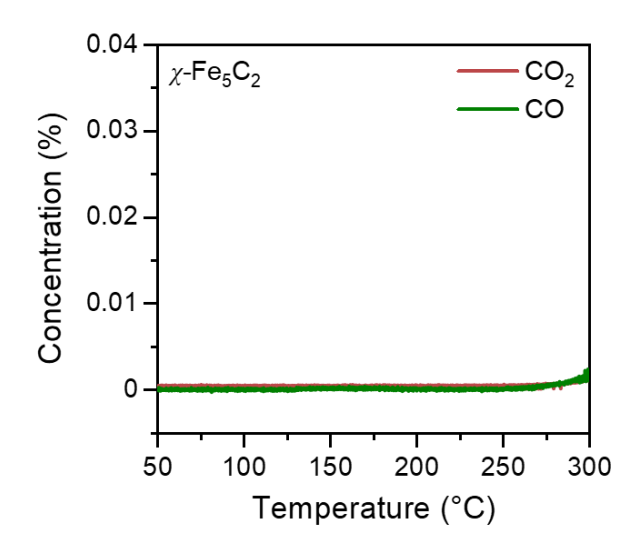


Fig. S38.

Blank control experiment of CO TP experiment of χ -Fe₅C₂. Reaction conditions: 50 mg χ -Fe₅C₂ (after pretreatment), 10 mL/min Ar, the temperature was raised from 50 °C to 300 °C at a rate of 10 °C/min.

Note: Since the catalyst was prepared by synthesis gas carburization, there will be carbon-containing species remaining on the catalyst surface after carburization. After the pretreatment (in 320 °C, Ar), it shows negligible CO or CO₂ formation below 300 °C.

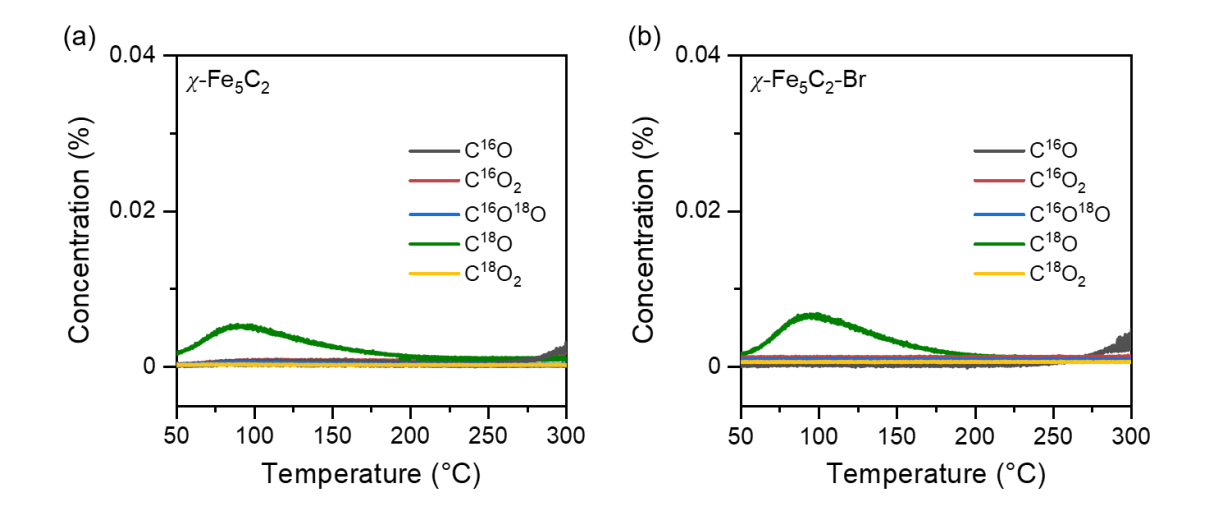


Fig. S39.

C¹⁸O TP desorption (TPD) results of χ -Fe₅C₂ (a) and χ -Fe₅C₂-Br (b) catalysts. Reaction conditions: 50 mg catalyst, 10 mL/min C¹⁸O/He/Ar = 5/10/85 was introduced at 50 °C and maintained for 20 min. The gas was switched to 10 mL/min Ar for 30 min until the C¹⁸O was fully purged. After that, the temperature was raised to 300 °C at a rate of 10 °C/min from 50 °C.

Note: Since the χ -Fe₅C₂ catalyst was made by carburization method using syngas, the pristine catalyst surface is rich in carbon-containing species, and the catalyst may also dissociate CO at high temperatures. Therefore, we conducted experiments using isotopic-labeled CO (18 CO).

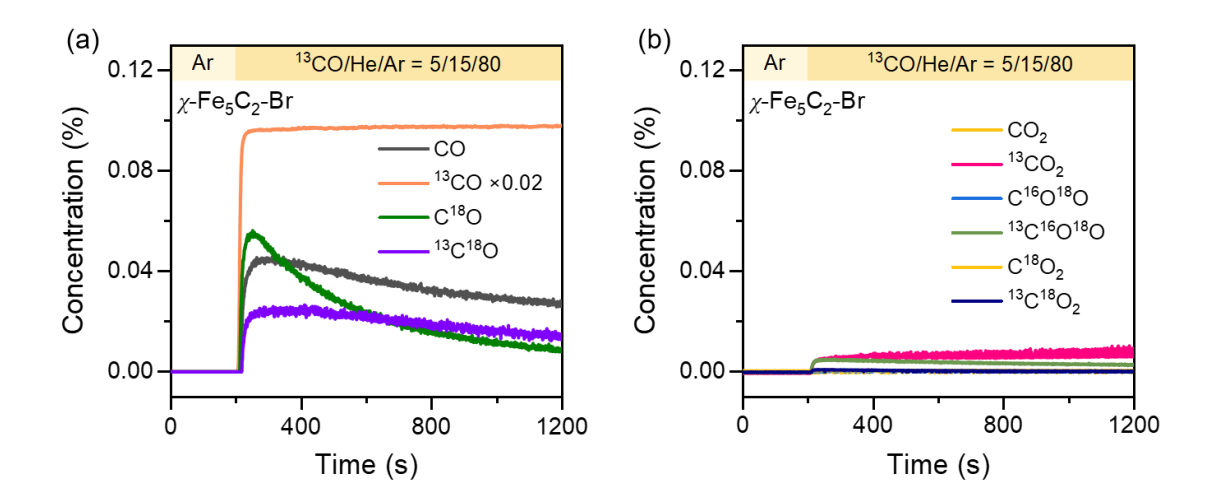


Fig. S40.

Ar \rightarrow C¹⁸O/He/Ar = 5/10/85 \rightarrow Ar \rightarrow ¹³CO/He/Ar = 5/10/85 TKA results of χ -Fe₅C₂-Br catalysts. Reaction conditions: 50 mg catalyst, 300 °C, after the introduction of 10 mL/min C¹⁸O/He/Ar = 5/10/85 for 20 min (after this process, the surface of catalyst was covered by ¹⁸O-containing species), the gas was switched to 10 mL/min Ar for 30 min until the C¹⁸O was fully purged, then switched to 10 mL/min ¹³CO/He/Ar = 5/10/85.

Note: CO may be either strongly adsorbed or undergo dissociation on the surface of χ -Fe₅C₂-Br catalyst. So, we firstly treat χ -Fe₅C₂-Br catalyst under C¹⁸O atmosphere to make an ¹⁸O-precovered surface. If CO does not dissociate on the catalyst surface, the C¹⁸O molecules would be left on the surface after C¹⁸O treatment. Subsequent treatment with ¹³CO would then only produce C¹⁸O and CO, without ¹³C¹⁸O (through competitive adsorption displacement).

However, if CO dissociation can occur, $C^{18}O$ would dissociate into $C^* + {}^{18}O^*$ (surface species) and remain on the surface during the $C^{18}O$ treatment. During the subsequent ${}^{13}CO$ treatment, ${}^{13}CO$ would dissociate into ${}^{13}C^* + O^*$. These surface C^* , ${}^{13}C^*$, O^* and ${}^{18}O^*$ species would then randomly recombine to produce CO, $C^{18}O$, and ${}^{13}C^{18}O$. This result confirmed that dissociative adsorption of CO did occur on the surface of χ -Fe₅C₂-Br catalyst.

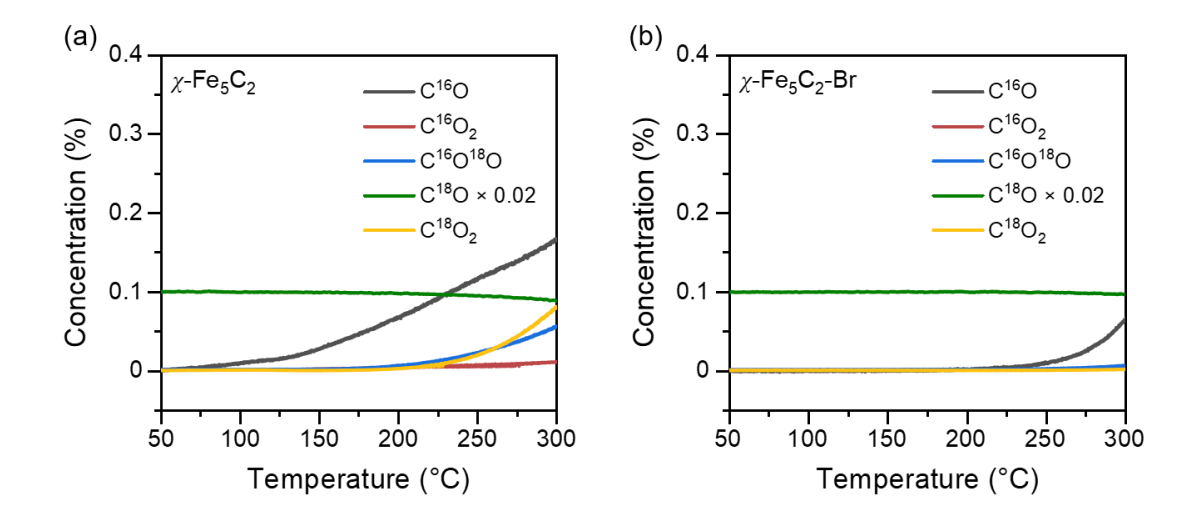


Fig. S41.

C¹⁸O temperature-programed surface reaction (TPSR) results of χ -Fe₅C₂ (a) and χ -Fe₅C₂-Br (b) catalysts. Reaction condition: 50 mg catalysts, 10 mL/min C¹⁸O/He/Ar = 5/10/85 was introduced at 50 °C and maintained for 20 min. After that, the temperature was raised to 300 °C at a rate of 10 °C/min from 50 °C.

Note: For χ -Fe₅C₂ catalyst, the formation of C¹⁶O¹⁸O and C¹⁸O₂ was observed starting at ~200 °C. In contrast, for χ -Fe₅C₂-Br catalyst, virtually no CO₂ (including C¹⁶O₂, C¹⁶O¹⁸O and C¹⁸O₂) was detected even at 300 °C. This further demonstrates the distinct Boudouard reactivity of the two catalysts. Besides, the formation of C¹⁶O and corresponding consumption of C¹⁸O also indicate the possible dissociation of CO on the surface of both catalysts at 300 °C. These results, combined with that in Fig. S38-S40 and Fig 3F, demonstrate that χ -Fe₅C₂-Br catalyst can still dissociate CO but is incapable of facilitating the Boudouard reaction at reaction conditions. This suggests that the key recombination step (CO* + O*) of the Boudouard reaction is inhibited.

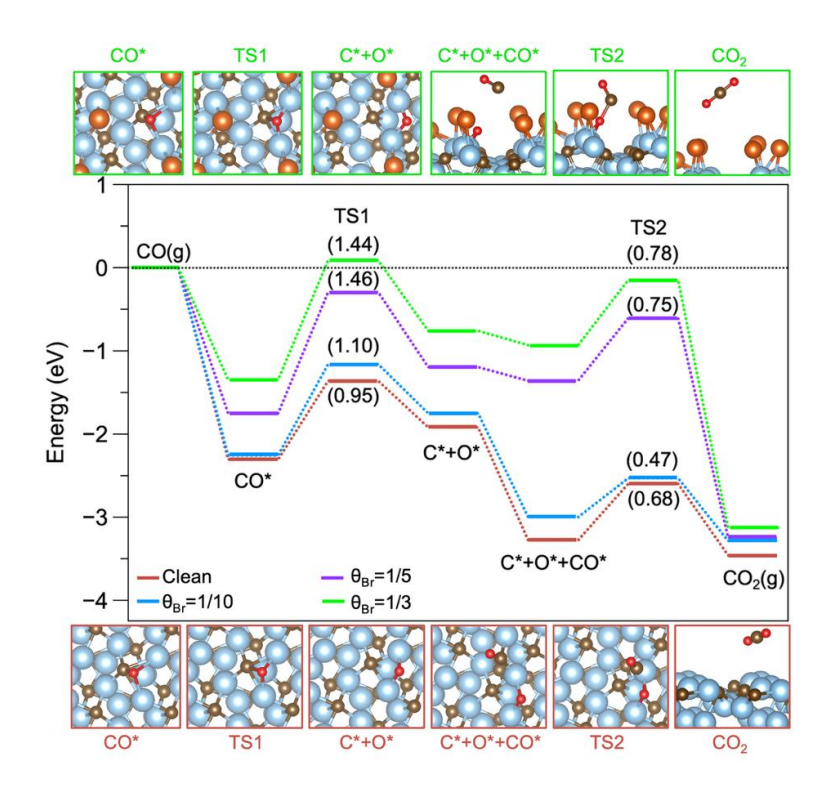


Fig. S42.

DFT-calculated Boudouard reaction energy profiles. Boudouard reaction pathways on χ -Fe₅C₂ (100) surfaces at different Br coverages ($\theta_{\rm Br}=0$ –1/3), demonstrating the substantial suppression of CO₂ formation upon Br modification.

Note: DFT calculations of Boudouard reaction on the χ -Fe₅C₂(100) surface reveal that, on the clean surface, the reaction proceeds readily, with low activation barriers of 0.95 eV for CO dissociation (TS1) and 0.68 eV for subsequent CO₂ formation (TS2), indicating a thermodynamically favorable and kinetically accessible pathway. However, increasing θ_{Br} significantly elevates these barriers, especially the CO₂ formation step, whose activation energy nearly doubles at $\theta_{Br} = 1/3$. Concomitantly, Br species strongly weaken the adsorption energy of CO, making the co-adsorption of a second CO molecule thermodynamically unfavorable. At $\theta_{Br} = 1/3$, adsorption of the second CO molecule becomes energetically unfavorable, significantly hindering its interaction with adsorbed O* species via the Langmuir-Hinshelwood (L-H) mechanism, thus further suppressing the Boudouard reaction pathway and CO₂

formation. This mechanistic transition underscores the critical role of Br in strongly inhibiting the Boudouard reaction pathway.

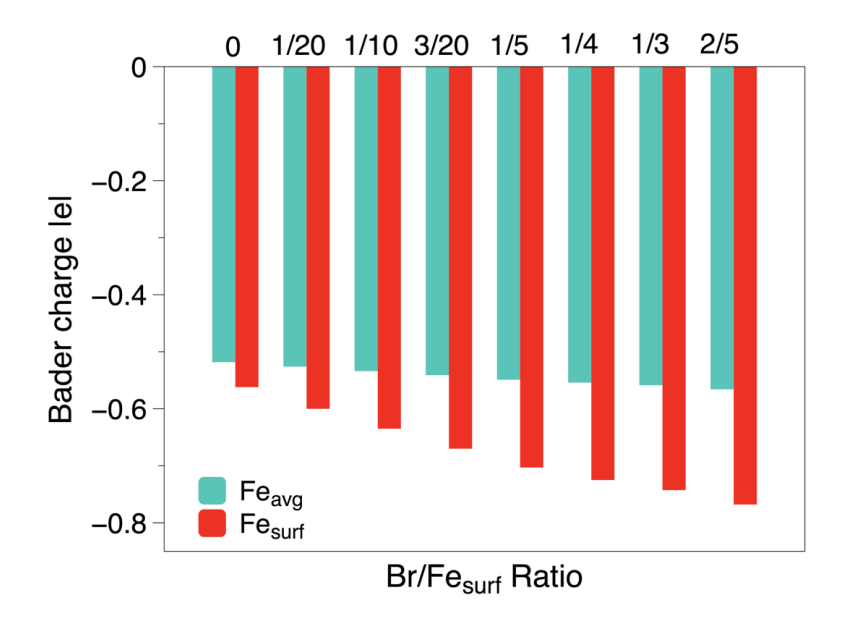


Fig. S43.

Bader charge analysis of surface Fe atoms on χ -Fe₅C₂ (100) as a function of Br coverage, indicating progressive electron depletion from Fe sites with increasing Br coverage.

Note: Figs. S43–S45 systematically illustrate how surface-bound bromine (Br) modulates electronic and steric properties of the χ -Fe₅C₂ (100) catalyst surface, thereby suppressing undesired secondary hydrogenation reactions. First, Bader charge analysis (Fig. S43) demonstrates progressive electron depletion of surface Fe atoms with increasing Br coverage, significantly altering their local electronic environment. Correspondingly, the Fe *d*-band center (Fig. S44) shifts downward in energy, weakening adsorption and reactivity of surface intermediates. Electron localization function (ELF) maps (Fig. S45) further confirm electron redistribution, showing enhanced electron localization around Fe-Br sites accompanied by depletion at adjacent catalytic sites. Optimized reaction intermediates (Figs. S46 and S47) reveal distinct structural changes upon Br modification. Without Br, intermediates and hydrogen atoms readily adsorb on clean Fe sites, favoring secondary hydrogenation (Fig. S46). Conversely, at high Br coverage ($\theta_{Br} = 1/3$, Fig. S47), Br atoms introduce significant steric hindrance, distorting the adsorption geometry, obstructing hydrogen approach, and thus effectively inhibiting secondary hydrogenation pathways. Together, these results indicate a

combined electronic and steric mechanism by which Br modification enhances catalytic selectivity.

Although olefin hydrogenation and H_2O dissociation are thermodynamically favorable, their corresponding reactants—olefins and H_2O —interact much more weakier with the Br-modified surface than CO. DFT calculations show that CO adsorption on the Br-modified χ -Fe₅C₂ surface is significantly stronger (-1.59 eV) than that of olefins (-0.45 eV), resulting in preferential site occupation by CO under reaction conditions. This site saturation effectively limits the access of olefins to hydrogenation-active surface Fe atoms. Consequently, olefins tend to desorb before undergoing secondary hydrogenation. In contrast, on unmodified surfaces, olefins exhibit stronger adsorption, enabling further hydrogenation and leading to increased paraffin formation (Fig. 4A).

A similar effect is observed for H₂O. In the absence of Br, H₂O readily absorbs and dissociates on iron oxide phases, facilitating CO₂ generation via the WGS reaction. Upon Br modification, however, surface Br atoms preferentially bind to Fe₃O₄ sites (with an adsorption energy of -3.74 eV), weakening the ability of these sites to adsorb and activate H₂O. This suppression of H₂O adsorption leads to diminished WGS activity and reduced CO₂ formation.

These results support the conclusion that the inhibition of olefin hydrogenation and H₂O dissociation arises primarily from adsorption competition and Br-induced site blocking, rather than intrinsic kinetic limitations. Further investigations of these effects are ongoing.

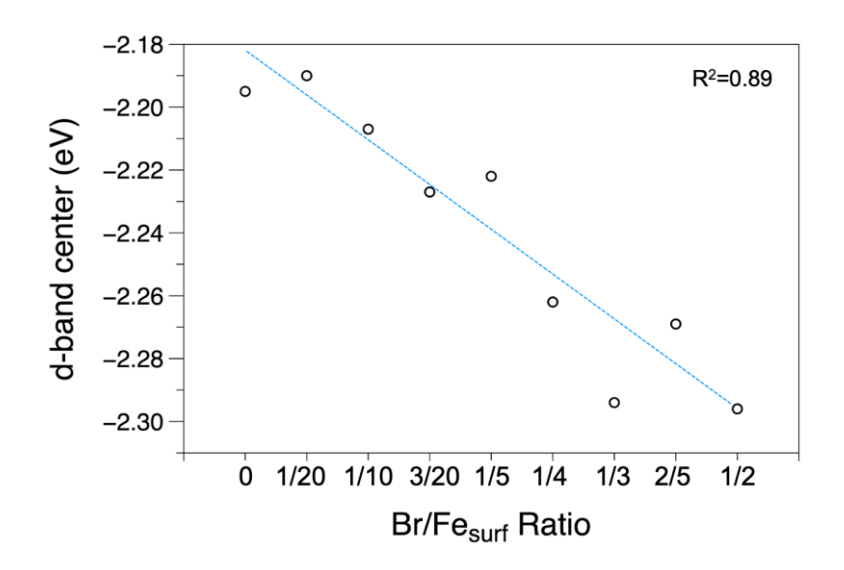


Fig. S44.

Relationship between Br coverage and the *d*-band center of surface Fe atoms on χ -Fe₅C₂ (100), showing a progressive downward shift in the *d*-band center with increasing Br coverage, consistent with reduced catalytic reactivity.

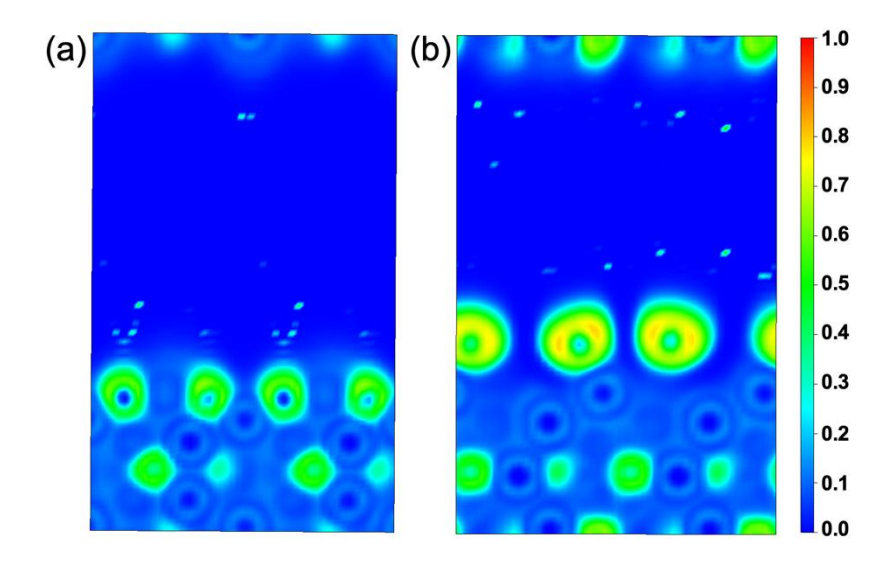


Fig. S45. Electron localization function of the bare χ -Fe₅C₂ (100) surface viewed along the [110] direction. Clean χ -Fe₅C₂ (100) surface (a) and surface with $\theta_{Br} = 1/3$ (b).

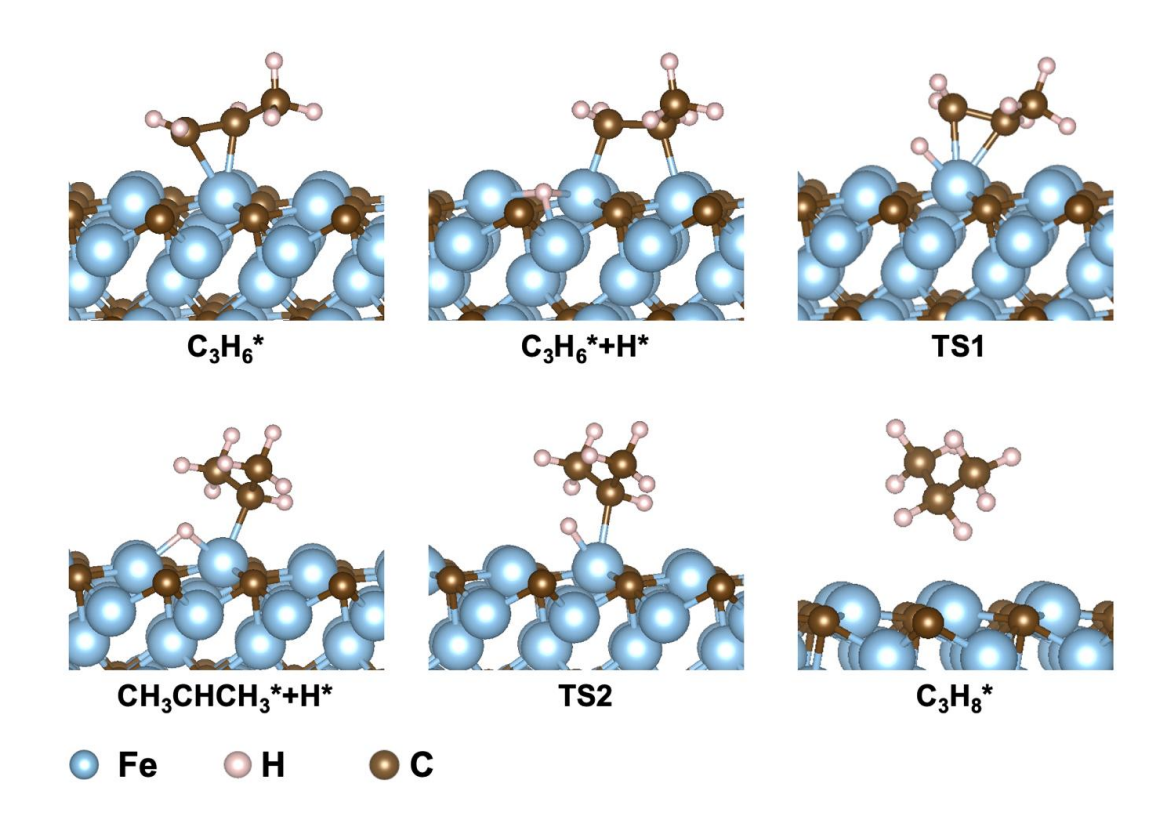


Fig. S46. Optimized structures of reaction intermediates along the CH₃CHCH₃ pathway on the bare χ -Fe₅C₂ (100) facet.

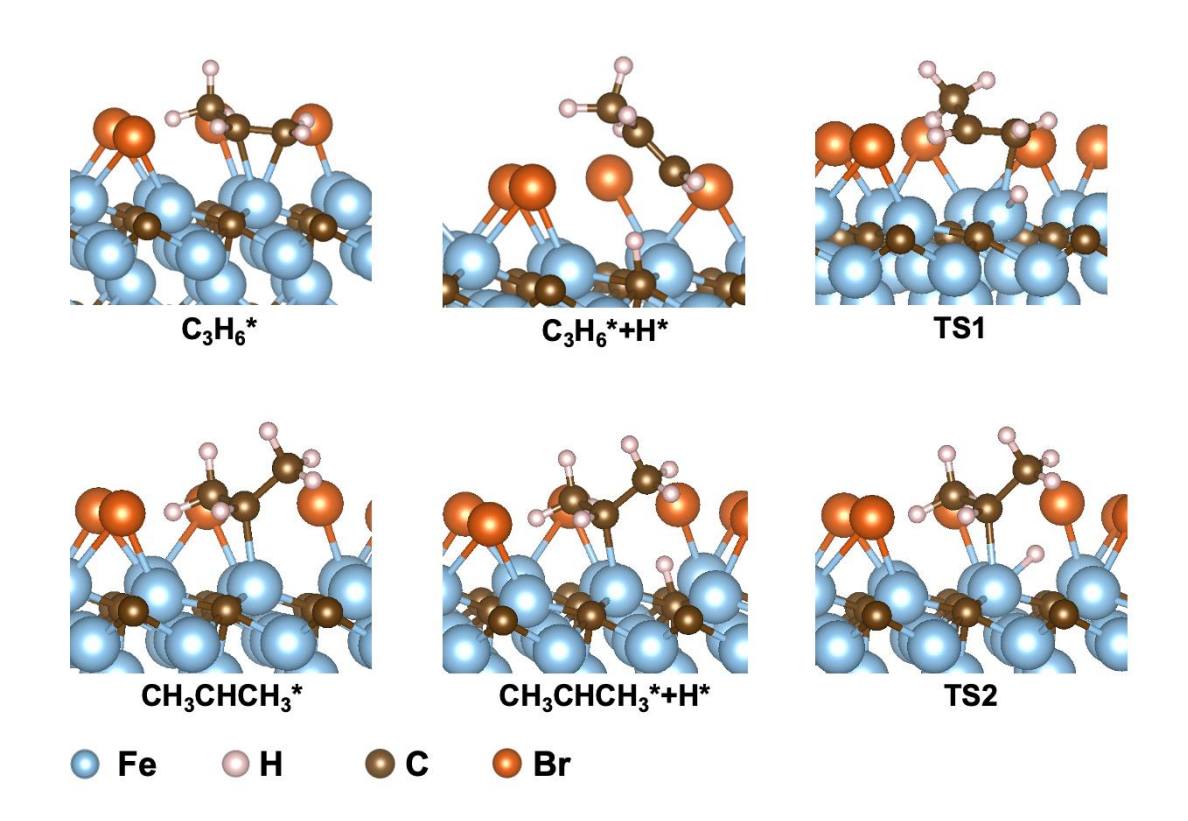


Fig. S47. Optimized structures of reaction intermediates along the CH₃CHCH₃ pathway on the χ -Fe₅C₂ (100) facet with $\theta_{Br} = 1/3$.

Table S1.Catalytic performance of χ -Fe₅C₂ catalyst with/without co-feeding CH₃X (X = F, Cl, Br, I).

Co-feeding	SV (mL·g _{cat} -1·h-1)	CO conv. (%)	CO ₂ (%)	Hydrocarbon (%)				o/p
component				CH ₄	C ₂ -C ₄ °	C_2 - C_4 =	C ₅₊	(C2-C4)
None	12000	93.3	31.4	16.4	17.2	21.6	44.9	1.3
CH ₃ F	12000	82.8	27.8	14.5	15.3	23.3	46.9	1.5
CH ₃ Cl	12000	64.8	9.4	6.6	3.6	26.0	63.8	7.3
CH ₃ Br	12000	28.9	1.1	12.9	6.7	38.5	42.0	5.8
CH ₃ I	12000	13.6	N.D. <i>a</i>	15.0	8.5	39.3	37.2	4.6

Reaction conditions: 100 mg catalyst, T = 300 °C, P = 20 bar, SV = 12000 mL·g_{cat}-l·h⁻¹, H₂/CO = 2 (molar ratio), co-feeding 20 ppm CH₃X (X = F, Cl, Br, I). Catalysts were pretreated at 280 °C and 1 bar for 6 h, SV = 12000 mL·g_{cat}-l·h⁻¹, H₂/CO = 2, co-feeding 20 ppm CH₃X (X = F, Cl, Br, and I).

a: CO₂ is not detectable in GC with co-feeding 20 ppm CH₃I at the reaction conditions above.

Table S2. Catalytic performance of χ -Fe₅C₂ catalyst in syngas co-feeding with different concentrations of CH₃Br (0–50 ppm).

CH ₃ Br	SV (mL·g _{cat} -1·h-1)	CO conv.	CO ₂ (%)	Hydrocarbon (%)				o/p
(ppm)				CH ₄	C2-C4°	C_2 - C_4 =	C ₅₊	(C_2-C_4)
0	60000	38.8	29.6	27.0	15.2	28.9	29.0	1.9
0	12000	89.4	38.3	23.5	25.2	22.9	28.4	1.0
3	12000	41.1	4.2	13.3	6.3	38.4	42.1	6.1
5	12000	37.8	2.8	12.1	5.3	37.1	45.4	7.0
10	12000	34.9	1.9	10.9	4.5	37.8	46.8	8.5
20	12000	33.5	1.2	9.6	3.8	36.5	50.1	9.6
50	12000	27.4	0.7	8.8	3.5	34.9	52.8	10.1

Reaction conditions: 100 mg catalyst, T = 300 °C, P = 10 bar, SV = 12000–60000 mL·g_{cat}-1·h⁻¹, H₂/CO = 2, co-feeding 0–50 ppm CH₃Br. Catalysts were pretreated at 280 °C and 1 bar for 6 h, SV = 12000 mL·g_{cat}-1·h⁻¹, H₂/CO = 2.

Table S3. Summary of CO₂ formation rate (r_{CO2}), FTS rate (r_{FTS}), olefins formation rate ($r_{olefins}$) and their corresponding percentage losses/increases over χ -Fe₅C₂ catalyst during syngas co-feeding with different CH₃Br concentrations (0–20 ppm).

CH ₃ Br (ppm)	r_{CO2} (mol·g _{cat} ⁻¹ ·h ⁻¹)	r _{FTS} (mol·g _{cat} ⁻¹ ·h ⁻¹)	rolefins (mol·gcat ⁻¹ ·h ⁻¹)	rco2 loss (%)	r _{FTS} loss (%)	rolefins increase (%)
0	0.0587	0.0724	0.0344	0	0	0
3	0.0029	0.0586	0.0504	95.0	19.0	46.2
5	0.0018	0.0553	0.0484	96.9	23.5	40.4
10	0.0011	0.0522	0.0467	98.1	27.8	35.6
20	0.0007	0.0512	0.0464	98.8	29.2	34.7

Reaction conditions: 100 mg catalyst, T = 300 °C, P = 10 bar, SV = 12000 mL·g_{cat}-1·h⁻¹, H₂/CO = 2, co-feeding 0–20 ppm CH₃Br. Catalysts were pretreated at 280 °C and 1 bar for 6 h, SV = 12000 mL·g_{cat}-1·h⁻¹, H₂/CO = 2.

Table S4. Catalytic performance of χ -Fe₅C₂-Br catalyst at different reaction pressures.

Press	SV	CO conv.	CO_2		o/p			
(bar)	$(mL\cdot g_{cat}^{-1}\cdot h^{-1})$		(%)	CH ₄	C2-C4°	C_2 - C_4 =	C5+	(C_2-C_4)
5	12000	26.4	0.8	7.8	2.5	32.3	57.4	13.1
10	12000	35.9	1.2	9.7	3.8	35.9	50.6	9.4
20	12000	35.5	1.4	12.3	6.7	39.7	41.3	6.0
30	12000	33.4	1.5	15.5	9.0	38.6	36.9	4.3
40	12000	35.5	2.0	17.4	11.4	38.0	33.2	3.4

Reaction conditions: 100 mg catalyst, T = 300 °C, P = 5–40 bar, SV = 12000 mL·g_{cat}⁻¹·h⁻¹, H₂/CO = 2, co-feeding 20 ppm CH₃Br. Catalysts were pretreated at 280 °C and 1 bar for 6 h, SV = 12000 mL·g_{cat}⁻¹·h⁻¹, H₂/CO = 2, co-feeding 20 ppm CH₃Br.

Table S5.Catalytic performance of χ -Fe₅C₂-Br catalyst at different reaction temperatures in 20 bar total pressure.

Temp	SV	CO conv.	CO_2]	o/p			
(°C)	$(mL \cdot g_{cat}^{-1} \cdot h^{-1})$	(%)	(%)	CH ₄	C2-C4°	C_2 - C_4 =	C5+	(C ₂ -C ₄)
280	12000	32.1	1.2	13.2	10.1	37.8	38.9	3.8
290	12000	29.0	1.2	13.0	7.5	40.0	39.4	5.3
300	12000	28.9	1.1	12.9	6.7	38.5	42.0	5.8
310	12000	31.1	1.2	12.6	5.9	38.5	43.0	6.5
320	12000	32.2	1.2	12.2	5.2	36.7	46.0	7.1
330	12000	34.6	1.6	12.0	4.2	34.5	49.2	8.2

Reaction conditions: 100 mg catalyst, T = 280-330 °C, P = 20 bar, SV = 12000 mL·g_{cat}-1·h⁻¹, H₂/CO = 2, co-feeding 20 ppm CH₃Br. Catalysts were pretreated at 280 °C and 1 bar for 6 h, SV = 12000 mL·g_{cat}-1·h⁻¹, H₂/CO = 2, co-feeding 20 ppm CH₃Br.

Table S6. Catalytic performance of χ -Fe₅C₂-Br catalyst at different reaction temperatures in 5 bar total pressure.

Temp	SV	CO conv.	CO ₂		Hydrocarbon (%)					
(°C)	$(mL \cdot g_{cat}^{-1} \cdot h^{-1})$		(%)	CH ₄	C2-C4°	C_2 - C_4 =	C5+	(C_2-C_4)		
280	12000	15.9	0.7	8.1	3.6	35.4	52.9	9.9		
300	12000	26.4	0.8	7.8	2.5	32.3	57.4	13.1		
320	12000	45.7	2.2	6.7	1.6	30.8	61.0	19.8		
340	12000	52.8	3.8	8.6	1.9	30.0	59.5	15.5		
360	12000	77.3	16.8	12.4	3.1	29.2	55.3	9.5		

Reaction conditions: 100 mg catalyst, T = 280-360 °C, P = 5 bar, SV = 12000 mL·g_{cat}⁻¹·h⁻¹, H₂/CO = 2, co-feeding 20 ppm CH₃Br. Catalysts were pretreated at 280 °C and 1 bar for 6 h, SV = 12000 mL·g_{cat}⁻¹·h⁻¹, H₂/CO = 2, co-feeding 20 ppm CH₃Br.

Table S7. Catalytic performance of χ -Fe₅C₂-Br catalyst at different space velocities.

SV	CO conv.	CO ₂		o/p			
$(mL\cdot g_{cat}^{-1}\cdot h^{-1})$	(%)	(%)	CH ₄	C2-C4°	C_2 - C_4 =	C5+	(C_2-C_4)
2000	56.9	2.6	6.2	2.3	28.3	63.2	12.5
4000	45.4	1.9	7.2	2.7	35.4	54.6	13.1
6000	41.4	1.7	7.8	2.5	32.9	56.9	13.3
8000	35.7	1.5	8.4	2.5	33.5	55.6	13.2
12000	29.7	1.3	8.7	1.9	24.4	65.0	12.5
16000	23.0	1.1	9.0	2.6	34.8	53.6	13.4
20000	20.7	1.3	9.7	2.9	39.1	48.3	13.7
30000	14.9	1.4	10.2	2.9	38.9	48.0	13.4

Reaction conditions: 100 mg catalyst, T = 300 °C, P = 5 bar, SV = 2000–30000 mL·g_{cat}-1·h·1, H₂/CO = 2, co-feeding 20 ppm CH₃Br. Catalysts were pretreated at 280 °C and 1 bar for 6 h, SV = 12000 mL·g_{cat}-1·h⁻¹, H₂/CO = 2, co-feeding 20 ppm CH₃Br.

Table S8.

Comparison of the catalytic performance of direct conversion of syngas to olefins.

E 4	Catalant	Т	P	H ₂ /CO	SV	СО	P	roduct	Selectivity	(%)	Olefins	Olefins	Ref.
Entry	Catalyst	(°C)	(MPa)	ratio	$(mL \cdot g_{cat}^{-1} \cdot h^{-1})$	conv. (%)	CO ₂	СН4	Olefins	Others	Yield (%)	$STY (g \cdot g_{cat}^{-1} \cdot h^{-1})$	KCI.
1	ZnCrO _x /MSAPO	400	2.5	2.5	7714	17.0	41.0	1.2	47.2 ^a	10.6	8.0 a	0.11	(12)
2	ZnZrO _x /SAPO-34	400	1	2	3600	9.5	45.0	3.3	34.7 ^a	17.1	3.3 ^a	0.02	(37)
3	ZnCrO _x /MOR	375	2.5	2.5	1857	12.0	45.0	2.8	46.8 a	5.5	5.6 ^a	0.02	(38)
4	ZnAl ₂ O ₄ +SAPO-34	390	4	1	12000	10.1	44.1	2.3	43.0 ^a	10.5	4.3 ^a	0.16	(39)
5	MnO _x /MSAPO	400	2.5	2	4800	8.5	41.0	1.2	46.7 ^a	11.1	4.0^{a}	0.04	(40)
6	ZnCrO _x /AIPO-18	390	4	1	1200	48.8	47.2	0.7	42.5 ^a	9.6	20.8^{a}	0.08	(41)
7	ZnCrO _x -GeAPO-18	430	6	2.5	1500	85.0	32.0	1.4	56.4 ^a	10.3	47.9 ^a	0.13	(13)
8	Fe-Zn-0.81Na	340	2	2	60000	50.2	33.3	9.3	49.1	8.3	24.6	3.08	(27)
9	Fe-Zn-0.81Na ^c	340	2	2	60000	77.2	23.8	9.7	58.4	8.1	45.1	4.06	(27)
10	FeMn@Si-c	320	3	2	4000	56.1	13.0	10.0	65.3	11.7	36.6	0.31	(11)
11	Fe/CNF	340	2	1	1500	88.0	42.0	7.5	30.2	20.3	26.5	0.12	(9)
12	Fe/α -Al ₂ O ₃	340	2	1	1500	80.0	40.0	6.6	31.8	21.6	25.4	0.12	(9)
13	Fe-K/NCNTs	300	0.1	1	4200	16.5	23.6	13.2	57.0	6.2	9.4	0.12	(42)
14	Fe/hNCNC	350	0.1	1	12000	3.5	39.4	15.2	42.8	2.6	1.5	0.06	(43)
15	Mn/Fe ₃ O ₄	320	1	1	4480	41.5	37.8	6.0	50.7	5.5	21.0	0.29	(32)

16	$Fe_{10}In/Al_2O_3$	400	0.5	2	7800	11.0	16.0	~22.0	45.0	~17.0	5.0	0.08	(44)
17	$Fe_3O_4@MnO_2\\$	280	2	1	3000	67.9	47.1	1.9	42.0	9.0	28.5	0.27	(45)
18	ε -Fe ₂ C-0.4Mn	300	2	2.5	20000	41.0	11.9	7.1	70.2	10.8	28.8	1.03	(16)
19	χ-Fe ₅ C ₂	250	2.3	1.5	20000	27.8	11.2	-	24.3 ^b	-	6.8^{b}	0.34	(10)
20	Mn- χ -Fe ₅ C ₂	250	3	1.5	5000	46.1	9.4	10.3	48.5 ^b	31.8	22.4 ^b	0.28	(10)
21	Mn-χ-Fe ₅ C ₂	250	2.3	1.5	28000	16.0	9.3	-	50.7 ^b	-	8.1 ^b	0.57	(10)
22	Mn-χ-Fe ₅ C ₂	290	2.5	1.5	60000	52.8	20.8	7.8	43.6 ^b	27.8	23.0 ^b	3.45	(10)
23	Mn- χ -Fe ₅ C ₂	290	2.5	1.5	30000	70.7	21.9	7.5	42.0 ^b	28.6	29.7 ^b	2.23	(10)
24	Mn- χ -Fe ₅ C ₂	320	2.5	1.5	60000	91.2	32.0	-	28.5 ^b	-	26.0 ^b	3.90	(10)
25	5Fe@C-II	260	2	1	250	17.2	4.6	5.6	11.4	78.3	2.0	0.00	(8)
26	Fe/Si/Cu/K-HCl	270	1.3	0.77	10000	20.0	15.0	4.3	72.7	8.1	36.3^{d}	0.51	(20)
27	Fe/Si/Cu/K-HBr	270	1.3	0.77	10000	30.0	33.0	3.7	55.1	8.2	41.3 ^d	0.58	(20)
28	CoMn	250	0.1	2	2000	31.8	47.3	2.6	32.0^{a}	18.0	10.2 a	0.04	(21)
29	Co_1Mn_3 - Na_2S	240	1	2	8000	18.0	3.0	4.0	77.7	15.3	14.0	0.23	(46)
30	0.5Na/CoMnAl@6.6Si	260	1	0.5	4000	13.5	16.7	4.3	61.1	17.9	8.2	0.14	(47)
31	Na-5%Ru(P)/SiO ₂	260	1	2	3000	65.3	2.7	1.9	73.7	21.7	48.1	0.30	(22)
32	Na-5%Ru/SiO ₂	260	1	2	3000	45.8	2.7	2.2	80.1	15.0	36.7	0.23	(22)
33	χ-Fe ₅ C ₂ -Cl	280	2	2	12000	57.9	6.1	5.5	76.5	11.9	44.3	1.11	
34	χ-Fe ₅ C ₂ -Cl	300	2	2	30000	51.2	8.5	7.7	73.7	10.0	37.8	2.36	This
35	χ -Fe ₅ C ₂ -C1	300	2	2	50000	41.8	7.8	10.5	69.8	11.9	29.2	3.04	work
36	χ -Fe ₅ C ₂ -Cl	310	2	2	80000	37.7	8.0	13.4	65.9	12.7	24.8	4.14	WOIK
37	χ -Fe ₅ C ₂ -Br	300	0.5	2	12000	26.4	0.8	7.7	85.0	6.5	22.3	0.56	

38	χ-Fe ₅ C ₂ -Br	320	0.5	2	12000	50.6	2.1	7.4	85.2	5.3	43.2	1.08	
39	χ-Fe ₅ C ₂ -Br	340	0.5	2	12000	54.2	3.9	7.9	82.8	5.4	44.8	1.12	
40	χ-Fe ₅ C ₂ -Br	300	0.5	2	2000	56.9	2.6	6.1	84.6	6.8	48.1	0.20	
41	χ-Fe ₅ C ₂ -Br	300	0.5	2	6000	41.4	1.7	7.7	84.3	6.3	34.9	0.44	

a: The values denote the selectivity and yield of lower olefins (C_2 - C_4 ⁼).

b: The values denote the selectivity and yield of C_2 - C_{10} linear α -olefins.

c: 8% CO₂ is included in the syngas feedstock (CO:H₂:CO₂:Ar=24:64:8:4).

d: The selectivity of olefins is estimated based on the selectivity of butene in the C₄ products.

Table S9.Br concentration, total mass, and volume of the aqueous and oil phases.

	Br concentration (mg/L)	Mass (g)	Volume (mL)
Aqueous phase a	5.8 ± 0.3	16.17	16.17
Oil phase b	0.5 ± 0.3	2.75	3.75

Reaction conditions: 100 mg catalyst, T = 300 °C, P = 10 bar, SV = 12000 mL·g_{cat}⁻¹·h⁻¹, H₂/CO = 2, co-feeding 20 ppm CH₃Br. Time-on-stream = 200 h (collection started after the induction period). Catalysts were pretreated at 280 °C and 1 bar for 6 h, SV = 12000 mL·g_{cat}⁻¹·h⁻¹, H₂/CO = 2, co-feeding 20 ppm CH₃Br. The aqueous and oil samples were collected from reaction products in a cold trap (wax formation was negligible during the reaction). The cold trap products were separated into aqueous and oil phases using a separatory funnel. The Br concentration in each phase was quantified by ion chromatography. The Br concentration reported in this table represents the averages of 3 replicate measurements.

- a: Aqueous phase density is approximately 1.000 g/mL.
- b: Oil phase density is approximately 0.733 g/mL.

Table S10.Fate of bromine under steady-state FTS reaction conditions.

	Br concentration	Br mass (mg)	Br content-out (%)
CH ₃ Br-in	20.0 (ppm)	17.121	-
CH ₃ Br-out	14.2 (ppm)	12.173	71.10
Aqueous phase-out	$5.8\pm0.3~(mg/L)$	0.094	0.55
Oil phase-out	$0.5\pm0.3~\text{(mg/L)}$	0.002	0.01

Reaction conditions: 100 mg catalyst, $T = 300 \,^{\circ}\text{C}$, $P = 10 \,\text{bar}$, $SV = 12000 \,\text{mL} \cdot \text{g}_{\text{cat}}^{-1} \cdot \text{h}^{-1}$, $H_2/\text{CO} = 2$, co-feeding 20 ppm CH₃Br. Time-on-stream = 200 h (collection started after the induction period). Catalysts were pretreated at 280 °C and 1 bar for 6 h, $SV = 12000 \,\text{mL} \cdot \text{g}_{\text{cat}}^{-1} \cdot \text{h}^{-1}$, $H_2/\text{CO} = 2$, co-feeding 20 ppm CH₃Br. Br concentration in the gas phase (as CH₃Br) was determined by mass spectrometry, while Br concentrations in the aqueous and oil phases were determined by ion chromatography. Mass of Br was calculated based on the corresponding concentrations and sample volumes. The Br content-out (%) represents the percentage of input Br recovered in each phase.

Table S11.Halogen concentration limits for various chemical processes and fuel applications.

	Halogen concentration limit (mg/L, ppm)
Hydroformylation	< 1, approximately
Polymer-grade olefins	< 1, approximately
Jet fuel	< 1 (ASTM D7566)
Marine fuel	< 50 (ISO 8217:2024)

Table S12.

Concentration of Br in catalysts was determined by ion chromatography and mass spectrometry.

Catalyst	Br content (wt%)	Br:Fe (mol%)	BET surface area (m²/g)	Surface Br:Fe ^a	Surface Br:Fe ^b
χ-Fe ₅ C ₂ ^c	-	-	-	-	-
χ-Fe ₅ C ₂ -Br-spent ^c	1.32 ± 0.09	1.02 ± 0.07	24.7	0.29 ± 0.02	0.55 ± 0.03
χ -Fe ₅ C ₂ -Br ^d	1.17	0.89	30.3	0.21	0.21

Reaction conditions: 100 mg catalyst, $T = 300 \,^{\circ}\text{C}$, $P = 10 \,^{\circ}\text{bar}$, $SV = 12000 \,^{\circ}\text{L} \cdot g_{\text{cat}}^{-1} \cdot h^{-1}$, $H_2/\text{CO} = 2$, co-feeding 20 ppm CH₃Br. Catalysts were pretreated at 280 °C and 1 bar for 6 h, $SV = 12000 \,^{\circ}\text{L} \cdot g_{\text{cat}}^{-1} \cdot h^{-1}$, $H_2/\text{CO} = 2$, co-feeding 20 ppm CH₃Br.

a: The surface Br:Fe ratio was calculated from the BET surface area data, assuming 14 Fe atoms/nm² (57). It has been assumed that the iron-containing particles consist fully of iron carbide at their surface.

b: The surface Br:Fe ratio was calculated from the surface-averaged mean particle size of the iron carbide nanoparticles from TEM data using the following equation, the density of χ -Fe₅C₂ (ρ = 7.57 g/cm³) and assuming 14 Fe atoms/nm² (57). It has been assumed that the iron-containing particles consist fully of iron carbide.

$$\langle d \rangle_{S} = \frac{\sum_{i=1}^{N} d_i^3}{\sum_{i=1}^{N} d_i^2}$$

In which d_i is the measured diameter of nanoparticle i and N is the total number of particles used for calculation (N > 150).

c: The Br content (wt%) was quantified by ion chromatography (IC), and the Br:Fe molar ratio was calculated based on the measured Br content. No Br was detected in the χ -Fe₅C₂ catalyst. Error bars represent the standard deviation (n = 3).

d: The Br content (wt%) was determined from the CH₃Br adsorption-reaction experiment by integrating the mass spectrum area, from which the Br:Fe molar ratio was subsequently calculated (Fig. S14).

Table S13. Fitting parameters for Mössbauer spectra of pristine χ -Fe₅C₂ catalyst.

Sample	IS (mm/s)	QS (mm/s)	Hhf (kOe)	Γ/2 (mm/s)	Area (%)	Phase
	0.37	0.12	25.29	0.44	39.44	χ -Fe ₅ C ₂ (A)
χ-Fe ₅ C ₂ -	0.35	-0.07	21.79	0.58	39.44	χ -Fe ₅ C ₂ (B)
pristine	0.30	-0.03	12.74	0.45	19.72	χ -Fe ₅ C ₂ (C)
	0.29	-1.04	-	0.29	1.39	Fe ³⁺ (spm)

Reaction conditions: catalysts were pretreated at 280 °C and 1 bar for 6 h, SV = 12000 mL· g_{cat}^{-1} ·h-1, H₂/CO =2.

Table S14. Fitting parameters for Mössbauer spectra of spent χ -Fe₅C₂ catalyst.

Sample	IS (mm/s)	QS (mm/s)	Hhf (kOe)	Γ/2 (mm/s)	Area (%)	Phase
	0.38	0.14	25.49	0.41	39.50	χ -Fe ₅ C ₂ (A)
χ-Fe ₅ C ₂ -	0.35	-0.07	21.86	0.52	39.50	χ -Fe ₅ C ₂ (B)
spent	0.24	-0.01	12.32	0.44	19.75	χ -Fe ₅ C ₂ (C)
	0.21	-1.10	-	0.29	1.25	Fe ³⁺ (spm)

Reaction conditions: 100 mg catalyst, T = 300 °C, P = 10 bar, SV = 12000 mL·g_{cat}-1·h⁻¹, H₂/CO =

2. Catalysts were pretreated at 280 °C and 1 bar for 6 h, SV = 12000 mL \cdot g_{cat}⁻¹·h⁻¹, H₂/CO =2.

Table S15. Fitting parameters for Mössbauer spectra of spent χ -Fe₅C₂-Br catalyst.

Sample	IS (mm/s)	QS (mm/s)	Hhf (kOe)	Γ/2 (mm/s)	Area (%)	Phase
χ-Fe ₅ C ₂ -Br- spent	0.37	0.12	25.36	0.48	32.48	χ -Fe ₅ C ₂ (A)
	0.36	-0.09	21.66	0.56	32.48	χ -Fe ₅ C ₂ (B)
	0.24	-0.03	12.51	0.43	16.24	χ -Fe ₅ C ₂ (C)
	0.40	-0.11	51.34	0.87	15.00	$Fe_3O_4(A)$
	0.70	-1.00	46.38	0.38	2.29	$Fe_3O_4(B)$
	0.26	1.11	-	0.29	1.49	Fe ³⁺ (spm)

Reaction conditions: 100 mg catalyst, $T = 300 \,^{\circ}\text{C}$, $P = 10 \,\text{bar}$, $SV = 12000 \,\text{mL} \cdot \text{g}_{\text{cat}}^{-1} \cdot \text{h}^{-1}$, $H_2/\text{CO} = 2$, co-feeding 20 ppm CH₃Br. Catalysts were pretreated at 280 °C and 1 bar for 6 h, $SV = 12000 \,\text{mL} \cdot \text{g}_{\text{cat}}^{-1} \cdot \text{h}^{-1}$, $H_2/\text{CO} = 2$, co-feeding 20 ppm CH₃Br.

Table S16.Curve-fit parameters for Fe *K*-edge EXAFS of Fe₅C₂ catalysts.

Catalyst ^a	Path	d (Å) b	C. N. ^c	Δ <i>E</i> ₀ (eV)	$\sigma^2 (\mathring{\mathbf{A}}^2)^d$	R-factor
χ-FesC2- pristine	Fe-C/O	1.96 ± 0.03	2.4 ± 0.5		0.004 ± 0.002	
	Fe-Fe	2.53 ± 0.01	10.0 ± 1.1	2 ± 2	0.015 ± 0.004	0.002
	Fe-Fe	2.64 ± 0.01	3.6 ± 0.4		0.010 ± 0.004	
	Fe-C/O	1.96 ± 0.03	2.1 ± 0.4		0.003 ± 0.002	
χ-Fe ₅ C ₂ - spent	Fe-Fe	2.54 ± 0.01	10.7 ± 1.1	3 ± 1	0.016 ± 0.004	0.001
	Fe-Fe	2.63 ± 0.01	3.6 ± 0.4		0.012 ± 0.004	
χ-Fe ₅ C ₂ - Br-spent	Fe-C/O	1.95 ± 0.03	2.1 ± 0.7		0.005 ± 0.003	
	Fe-Fe	2.44 ± 0.01	2.0 ± 0.1	2 ± 2	0.008 ± 0.002	0.005
	Fe-Fe	2.59 ± 0.01	8.0 ± 0.4		0.012 ± 0.004	

a: The data ranges used in these fittings are $3.0 \le k \le 13.0 \text{ Å}^{-1}$ and $1.0 \le R \le 3.0 \text{ Å}$. S_0^2 was fixed at 0.782, obtained from the Fe foil measured at the same time. The number of variable parameters in each fitting is out of total of 12.4 independent data points.

b: The coordination distance. The distances for Fe-O and Fe-Fe are from the crystal structure of χ -Fe₅C₂ (C2/c, ICSD collection code 423886).

c: Average coordination number.

d: Debye-Waller factor.

Table S17.Fitting parameters of O 1s XPS of Fe₃O₄ after 400 °C Ar pretreatment and in 1 mbar H₂O.

Condition	Component	Position (eV)	FWHM (eV)	Percentage (%)
	O _{lattice}	530.20	1.32	89.9
r.tUHV	$\mathrm{OH}_{\mathrm{ads}}$	531.57	1.19	10.1
	$\mathrm{H_2O_g}$	-	-	-
	O _{lattice}	530.18	1.31	75.9
1 mbou II O ma	$\mathrm{OH}_{\mathrm{ads}}$	531.53	1.44	12.2
1 mbar H ₂ O_r.t.	H_2O_{abs}	533.05	1.51	6.1
	$\mathrm{H}_2\mathrm{O}_\mathrm{g}$	535.16	0.85	5.8
	O _{lattice}	530.16	1.33	83.3
$1~mbar~H_2O_100~^{\circ}C$	$\mathrm{OH}_{\mathrm{ads}}$	531.57	1.46	13.0
	$\mathrm{H}_2\mathrm{O}_\mathrm{g}$	535.16	0.84	3.7
	O _{lattice}	530.25	1.40	78.9
$1~mbar~H_2O_200~^{\circ}C$	$\mathrm{OH}_{\mathrm{ads}}$	531.57	1.36	18.5
	$\mathrm{H_2O_g}$	535.16	0.78	2.7
	O _{lattice}	530.27	1.40	71.4
1 mbar H_2O_250 °C	$\mathrm{OH}_{\mathrm{ads}}$	531.57	1.55	26.4
	$\mathrm{H_2O_g}$	535.16	0.76	2.2

Note: Under a water vapor pressure of 1 mbar, quantitative analysis of NAP-XPS spectra revealed a notable increase in the surface hydroxyl species (OH_{ads}) with increasing temperature. Specifically, the OH_{ads} increased from 10.1% at room temperature to 26.4% at 250 °C, indicating a thermally promoted dissociation of H_2O on the Fe_3O_4 surface at elevated temperatures.

Table S18.Fitting parameters of O 1s XPS of Fe₃O₄-Br after 400 °C Ar pretreatment and in 1 mbar H₂O.

Condition	Component	Position (eV)	FWHM (eV)	Percentage (%)
	O _{lattice}	530.18	1.30	90.3
r.tUHV	$\mathrm{OH}_{\mathrm{ads}}$	531.57	1.24	9.7
	$_{\mathrm{H_2O}_{\mathrm{g}}}$	-	-	-
	O _{lattice}	530.23	1.29	78.5
11 11 04	$\mathrm{OH}_{\mathrm{ads}}$	531.53	1.24	9.3
1 mbar H ₂ O_r.t.	H_2O_{abs}	533.05	1.89	7.1
	H_2O_g	535.16	0.86	5.2
	O _{lattice}	530.20	1.31	84.0
$1~mbar~H_2O_100~^{\circ}C$	$\mathrm{OH}_{\mathrm{ads}}$	531.57	1.55	12.0
	H_2O_g	535.16	0.98	4.0
	Olattice	530.18	1.35	84.4
$1~mbar~H_2O_200~^{\circ}C$	$\mathrm{OH}_{\mathrm{ads}}$	531.57	1.36	11.6
	H_2O_g	535.16	0.95	3.9
	Olattice	530.19	1.39	83.1
$1~mbar~H_2O_250~^{\circ}C$	$\mathrm{OH}_{\mathrm{ads}}$	531.57	1.38	13.5
	H_2O_g	535.16	0.91	3.4

Note: Under a water vapor pressure of 1 mbar, quantitative analysis of NAP-XPS spectra revealed only a slight increase in surface OH_{ads} species on Fe_3O_4 -Br with increasing temperature. Specifically, the OH_{ads} increased from 9.7% at room temperature to 13.5% at 250 °C. This limited variation indicates that H_2O dissociation is significantly inhibited on the Fe_3O_4 -Br surface even at 250 °C.